Surface & Coatings Technology 474 (2023) 130098

Contents lists available at ScienceDirect

Surface & Coatings Technology

journal homepage: www.elsevier.com/locate/surfcoat

Full length article

Tribological and electrochemical performances of HVOF sprayed NbC-NiCr coatings

Larissa Rossi Gehlen [a,b,c], Giovanni Bolelli [a,d,e,*], Pietro Puddu [c], Enrico Forlin [f], Alberto Colella [f], Giuseppe Pintaude [b], Luca Lusvarghi [a,d,e]

[a] Dipartimento di Ingegneria "Enzo Ferrari", Università di Modena e Reggio Emilia, Via Pietro Vivarelli 10/1, 41125 Modena, MO, Italy
[b] Universidade Tecnológica Federal do Paraná, Curitiba, Paraná, Brazil
[c] Il Sentiero International Campus S.r.l., Via Friuli 11, 36015 Schio, VI, Italy
[d] InterMech-MO.RE., Centro Interdipartimentale per la Ricerca Applicata e i Servizi nel Settore della Meccanica Avanzata e della Motoristica, Università di Modena e Reggio Emilia, Via Pietro Vivarelli 2, 41125 Modena, MO, Italy
[e] Consorzio Interuniversitario Nazionale per la Scienza e Tecnologia dei Materiali (INSTM), Local Unit: Università di Modena e Reggio Emilia, Via Pietro Vivarelli 10/1, 41125 Modena, MO, Italy
[f] MBN Nanomaterialia S.p.A., Via G. Bortolan, 42, 31050 Vascon di Carbonera, TV, Italy

ARTICLE INFO

Keywords:
Niobium carbide
High-Velocity Oxygen Fuel (HVOF)
Hardmetal coating
Sliding wear
Abrasive wear
Electrochemical corrosion

ABSTRACT

A wide range of mechanical parts are protected against wear and corrosion by thermally sprayed WC- or Cr_3C_2-based hardmetals. However, little is known about the potential of other hardmetal coating formulations. Since promising results were obtained with bulk NbC-based hardmetal cutting tools, in this work we investigated NbC-based coatings, which have not been reported yet in the literature. NbC particles were homogeneously dispersed with volume fractions of 25 % and 40 % in a Ni-20wt.%Cr matrix by mechanical alloying, and the resulting powders were sprayed onto stainless steel substrates by the High-Velocity Oxygen Fuel (HVOF) process.

Irrespective of the process parameters, the coatings exhibit low porosity (<1 vol%) and hardness values of about 900 $HV_{0.3}$ (NbC-25NiCr) and 1000 $HV_{0.3}$ (NbC-40NiCr). The composition with higher amount of NbC phase is less hard because its greater brittleness results in cracking during indentation.

The sliding wear resistance of the NbC-based coatings, tested by ball-on-disc tribometry from room temperature up to 600 °C, is generally intermediate between that of WC-CoCr and Cr_3C_2-NiCr references, and it is usually comparable to that of TiC-NiCr, another type of alternative hardmetal coating, tested in our previous work. Though the NbC-NiCr coatings exhibited limited three-body abrasion resistance due to the occurrence of some brittle fracture together with ductile grooving, they offer a particularly interesting performance at 400 °C, with lower wear rates than Cr_3C_2-NiCr and TiC-NiCr.

Additionally, the NbC-NiCr coatings tested in this work, especially the one with 40 vol% matrix phase, exhibit excellent corrosion resistance. Corrosion current densities (~0.1 μA/cm^2) and passive current densities (<1 μA/cm^2), both obtained by electrochemical polarization tests, were lower than the corresponding values found for all reference coatings (WC-CoCr, Cr_3C_2-NiCr and TiC-NiCr),

Thus, the NbC-NiCr coatings are promising for applications where a good balance between corrosion resistance and wear resistance over a range of temperatures is required.

1. Introduction

Effective performance of industrial components subject to severe working conditions, involving for example structural loads coupled with tribological contacts, can only be achieved by the combination of different materials. For instance, a temperature increase can lead to unacceptably reduced wear resistance, because it changes the properties of all tribo-elements [1], including the nature of third bodies [2]. If components are simultaneously subject to high temperatures and harsh environments, it is additionally necessary to focus on corrosion behaviour. In the case of simultaneous occurrence of wear and corrosion, the synergism of these phenomena can dramatically reduce the performance

* Corresponding author at: Dipartimento di Ingegneria "Enzo Ferrari", Università di Modena e Reggio Emilia, Via Pietro Vivarelli 10/1, 41125 Modena, MO, Italy.
E-mail address: giovanni.bolelli@unimore.it (G. Bolelli).

https://doi.org/10.1016/j.surfcoat.2023.130098
Received 30 August 2023; Received in revised form 10 October 2023; Accepted 11 October 2023
Available online 13 October 2023

of materials [3].

Considering the difficulty to satisfy all demands, a materials designer must find a proper balance among issues. Applying solutions based on surface engineering is an excellent option to find this balance [4], especially since some of them are analogues of the bulk materials approach in terms of the microstructure. A recognized example is the use of cemented carbides deposited by high-velocity oxygen fuel (HVOF) [5].

WC-Co based cemented carbides, also known as hardmetals, have long been known for their use in bulk (sintered) form as cutting tools [6], providing a unique combination of hardness and toughness due to the good balance of hardness and toughness of WC itself and, most of all, to the excellent interface wetting of metallic cobalt towards WC [7,8].

Based on these experiences, WC-Co based hardmetals with slightly adjusted composition have also become very popular as feedstock materials for thermally sprayed (generally, HVOF-sprayed) coatings, providing wear and corrosion protection in a variety of applications like ball valves, papermaking and steelmaking rolls, hydraulic turbine parts, pump parts, hydraulic rods, etc. [5,9].

Despite the success in applying tungsten carbides by HVOF, there is an ascending worry related to the use of critical raw materials, and both tungsten and cobalt can be included in this class [10,11]. A solution could be the development of new binder phases to replace cobalt, keeping WC as the hard phase. However, the use of iron is restricted by the low solubility of WC in Fe. According to Fernandes and Senos, at the respective eutectic temperatures, the solubility of WC in Fe is lower than in Co [12]. The data published by Guillermet [13] indicates that the solubility of WC in Fe at 1200 °C, which is close to the reported eutectic temperature of 1143 °C [12], is 10 wt%, whilst Co can dissolve around 19 wt% of WC at the eutectic temperature of 1320 °C [14], and, according to the WC-Co "pseudo-binary" phase diagram [14], at 1200 °C the solubility of WC in Co is around 15 wt%, which is still higher than that in Fe at the same temperature. Lower solubility also limits the wettability at the carbide-matrix interface. In the case of nickel, the limit is the maximum solubility of Carbon, <5.5 wt% [15]. Therefore, changing the carbide composition can open up more flexible processing routes to use binders different from cobalt. The use of TiC (which is harder than WC) was reported by various authors, most notably by Berger et al. [5,16–19], who investigated a variety of TiC-based hardmetals focusing also on ways to enhance the carbide-matrix wettability, and by Bobzin et al. [20,21], who studied metal-matrix composite coatings reinforced by TiC particles in a comparatively lower amount than in the hardmetals tested by Berger et al.. The authors of the current article also studied TiC-based coatings using different binders and deposition processes [22,23].

Bolelli et al. [22] studied two formulations – TiC-25NiCr and TiC-40NiCr – focusing on their corrosion and sliding wear resistance. The coatings were deposited using HVOF or HVAF processes, and the sliding wear was studied at room temperature and at 400 °C. The compositions performed differently: the one with higher carbide content was potentially suitable for high temperatures, while the one with higher binder content performed better at room conditions. Nonetheless, none of these compositions attained the same sliding and abrasive wear resistance of the WC-based coatings tested as a benchmark, although they did show better sliding wear resistance than Cr_3C_2-NiCr. Thus, it was concluded that the research should be continued by attempting other formulations to get a more suitable balance between different temperatures.

In a subsequent study, Testa et al. [23] modified both carbide and binder formulations and also added an intermediate composition, TiC-33NiCr. A certain fraction of WC was added in a TiC-WC-NiCr formulation, while iron was introduced into NiCr to compose a new metallic phase in a TiC-FeNiCr hardmetal. Unfortunately, the intermediate composition did not improve the previous results, and adding WC was rather ineffective. Nonetheless, the introduction of iron showed good potential in terms of corrosion: the TiC-FeNiCr was more resistant than traditional WC-4Cr10Co and Cr_3C_2-NiCr solutions.

Considering the findings of Bolelli et al. [22] and Testa et al. [23], and in particular the fact that the limitations of TiC-based hardmetals cannot be overcome just by adding some WC to them, one can figure out another carbide composition as the hard phase. NbC is softer than WC but can offer a balance between high-temperature wear resistance and corrosion resistance. The literature on thermally sprayed NbC-based coatings is scarce. Nonetheless, investigations on bulk hardmetal formulations showed the potential of NbC to provide wear resistance over a range of temperatures.

For instance, Woydt et al. showed that NbC-based sintered hardmetals are promising for cutting tool applications, approaching [24] or surpassing [25,26] the performance of WC-Co grades, e.g. in dry cutting and in dry abrasion tests. Potential cost advantages due to lower density (hence, lower material mass per unit coating area for a given thickness), as well as promising high-temperature performances related to the high refractoriness of NbC (its mechanical properties decrease less markedly with temperature), and to the stability of the corresponding oxide phase (Nb_2O_5) when compared to WO_3 [25] are other notable upsides. Rather importantly for a coating application, NbC has higher thermal expansion coefficient than WC [25]. Therefore, a NbC-based hardmetal coating is expected to exhibit a smaller mismatch in thermal expansion coefficient with ordinary metal substrates (e.g. steels) than do WC-based ones, which is another important factor limiting the high-temperature usability of WC-based hardmetals [27].

Another interesting feature of NbC is that it was found to bond even better to Ni- than to Co-based matrices [25,26], which is especially interesting in light of the potential replacement of cobalt with less toxic materials. Further, despite both niobium and tungsten being critical raw materials because of their strategic nature coupled with supply insecurity [28], the overall reserves of niobium are estimated to be much larger than those of tungsten [25], and the world's largest producers of these two elements are not the same [29], which could contribute to the strategic sustainability of this material [30].

NbC-based coatings have been deposited using different processes than HVOF and have been found to be effective in improving the wear and corrosion resistances of cast irons applied for automotive applications. Using thermo-reactive diffusion, Amaya et al. [31] found a significant impact on corrosion resistance against diesel and palm biodiesel exposures when NbC was applied to grey cast iron. Another interesting finding is the US patent for brake disks based on NbC and Cr_3C_2 powders, cladded onto cast iron using laser technology [32]. These components are subject to wear and corrosion environments at high temperatures, that is, to the complex synergism described above. Therefore, there are many indications that NbC-based coatings are a promising solution to meet these requirements better than other carbide types.

The primary goal of our investigation is to deposit NbC-based hardmetals using thermal spraying processes, to achieve a proper balance of diverse tribological and electrochemical performances. We have chosen the same formulations of the binder phase previously investigated by Bolelli et al. [22] with TiC-based hardmetals, namely 25 vol% and 40 vol% of a Ni-20wt.%Cr alloy, so that it is possible to compare all performances of the NbC-based formulations with the previous TiC-based coatings and the conventional WC-10Co4Cr and Cr_3C_2-NiCr references.

2. Experimental

2.1. Feedstock powders and coating deposition

Two compositions of feedstock material powders, designated as NbC-25NiCr and Nb-40NiCr, with nominal compositions of 75vol%NbC - 25 vol%(Ni-20wt%Cr) and 60 vol% NbC - 40 vol%(Ni-20 wt%Cr), were produced by MBN Nanomaterialia (Vascon-TV, Italy) via mechanical alloying in the solid state using a proprietary, industrial high-energy ball milling (HEBM) process, starting from NbC powder with particle size of

Table 1
HVOF process parameters for the deposition of NbC-NiCr coatings.

	NbC-NiCr coatings					WC-CoCr (WOKA 3652)
Parameter sets	R1	R2	R3	R4	R5	/
Fuel (H_2) Flow rate – [SLPM]	574	615	635	553	594	666
O_2 Flow rate – [SLPM]	201	221	214	214	188	234
Air flow rate – [SLPM]	274	266	274	274	266	235
Standoff distance – [mm]	250	250	250	250	250	240
Powder feed rate – [g/min]	30	30	30	30	30	60
N° of cycles	27	27	27	27	27	24
Transverse speed – [mm/s]	750	750	750	750	750	750
Pitch distance – [mm]	5	5	5	5	5	6

1–1.5 μm (provided by CBMM – Companhia Brasileira de Metalurgia e Mineração) and a Ni–20wt%Cr alloy. After processing, the powders were sieved and air classified in the particle size range 10–38 μm and packed and sealed under vacuum, to avoid oxidation. MBN Nanomaterialia provided nominal chemical compositions and particle size distribution values. The NbC-25NiCr and NbC-40NiCr compositions respectively presented $d_5 = 18$ μm, $d_{50} = 32$ μm, $d_{95} = 53$ μm and $d_5 = 11$ μm, $d_{50} = 26$ μm, $d_{95} = 49$ μm.

The feedstock powders produced by HEBM and a commercial reference of composition WC-10wt%Co-4wt.%Cr (WOKA 3652, Oerlikon Metco WOKA GmbH, Barchfeld, Germany), denoted as WC-CoCr in the following, were thermally sprayed onto AISI 304 stainless steel plates of 60 mm length × 25 mm width × 3 mm thickness using a Diamond Jet 2600 HVOF hybrid torch (Oerlikon Metco, Wohlen, Switzerland) operated with a mixture of hydrogen (H_2), oxygen (O_2) and air. Before thermal spraying, the plates were manually grit-blasted using brown alumina abrasive of 36 mesh and pressure of 5.5 bar (which gave the substrate an eventual surface roughness Ra ≈ 6 μm), ultrasonically cleaned in acetone and pre-heated at 60 °C in a drying oven.

NbC-40NiCr coatings were produced by HVOF, using five sets of parameters (named "R1" to "R5" in Table 1) characterized by different flow rates of H_2, O_2 and air, whilst only sets "R1" and "R2" were employed for the NbC-25NiCr composition. The parameter sets were determined based on previous experiences of HVOF processing with hardmetal coatings [22,33,34]. The deposition efficiency was calculated as the ratio between the mass of powder effectively deposited onto the steel plates (obtained by weighing the plates on an electronic scale with a precision of ±0.01 g before and after spraying) and the overall powder mass sprayed towards the plates (calculated based on the powder feed rate and the torch/substrate kinematics – see Table 1).

Other reference coatings sprayed by HVOF in previous work by the group were also analysed in this study: Cr_3C_2-25 wt%(Ni-20wt.%Cr) (WOKA 7102, Oerlikon Metco WOKA GmbH, Barchfeld, Germany), with spray parameters listed in [33], and two TiC-NiCr compositions, namely 75vol %TiC - 25 vol%(Ni-20wt%Cr) ([22], parameter set #5) and 60 vol % TiC - 40 vol%(Ni-20wt%Cr) ([22], parameter set #6).

2.2. Powders and coating characterization

Particle size characterizations, thermogravimetric analysis, phase composition analysis by X-ray diffraction, and cross-sectional observations were performed on the NbC-25NiCr and NbC-40NiCr powders. Particle size distribution was measured by laser diffraction (Mastersizer 2000, Malvern Instruments, Malvern, UK) using the water dispersion technique (Hydro 2000-S, Malvern Instruments). The oxidation behaviour of the particles was evaluated through simultaneous differential thermal analysis (DTA) and thermo-gravimetry (TG) in air (STA409, Netzsch, Selb, Germany), in which approximately 100 mg of powder sample was inserted in an alumina crucible, with another empty crucible as reference, and heated to 1290 °C at a rate of 10 °C/min. The phase composition was determined by X-ray diffraction (XRD: X'Pert PRO diffractometer, PANAlytical, Almelo, Netherlands). For this analysis, patterns were acquired in a range of $20° \leq 2\theta \leq 90°$ using Cu-Kα radiation (wavelength: 1.540598 Å) from a conventional source operated at 40 kV, 40 mA, a step size of 0.017° and a counting time of 120 s/step.

After embedding the powders in a two-component epoxy resin at room temperature and appropriate grinding and polishing procedures using SiC papers (up to 2500 mesh), 3 μm-polycrystalline diamond slurry, and colloidal silica suspension, the microstructure was observed through a scanning electron microscope (SEM: Nova NanoSEM 450, FEI – Thermo Fisher Scientific) equipped with an energy dispersive X-ray detector (EDX – Quantax-200, Bruker). Quantitative EDX analyses were performed by acquiring spectra at 15 kV e-beam acceleration voltage over the entire field-of-view imaged at 400×, with the exclusion of carbon and oxygen which are also contained in the mounting resin. The results obtained are presented as mean ± standard deviation from three measurements. To quantify oxygen and carbon, elemental analyses were performed by the oxygen combustion method (TCH600 instrument, LECO Corporation, St. Joseph, MI, USA) and the inert gas fusion technique (CS230 instrument, LECO Corporation), respectively, according to the procedure previously described in [22]. The overall results by EDX and by elemental analyses were then renormalized to 100.

The coatings also had phase compositions and cross-sectional microstructures characterized by X-ray diffraction and scanning electron microscopy techniques using the same equipment and methodologies applied to the powders. However, the coated samples were hot embedded in a phenolic resin. Again, quantitative EDX spectra were acquired in large-area scans (400× magnification) for each coating sample using an e-beam with an energy of 15 keV. In this case, the quantification also included carbon and oxygen.

The thickness and porosity of the coatings were measured by image analysis (ImageJ software, NIH, Bethesda, MA, USA) on an SEM micrograph acquired at 400× magnification (6 individual thickness readings) and eight SEM micrographs acquired at 3000× magnification, respectively.

Microhardness analyses were performed on the same cross-sections. For this test, a depth-sensing Vickers micro-indenter (Micro-Combi^3, Anton Paar TriTec, Corcelles, CH) was used. A total of 20 indentations were performed on each sample, using a maximum load of 3 N (≈ 300 gf), a loading/unloading rate of 4.5 N/min and a holding time of 15 s at the maximum load. The measurement procedure, calibration, and data analysis were carried out according to the ISO 14577 [35] standard, thus making it possible to present the results in terms of indentation hardness (H_{IT}) and to convert them to Vickers hardness ($HV_{0.3}$), using the geometrical relation between projected and actual contact area of a Vickers indenter.

2.3. Dry sliding wear resistance

Dry sliding wear tests were carried out on the samples of NbC-NiCr coatings and the reference coatings TiC-25NiCr, TiC-40NiCr, WC-CoCr, and Cr_3C_2-NiCr, previously ground with diamond papers and polished with 3 μm-polycrystalline diamond slurry to achieve a roughness Sa < 0.1 μm. The rotating ball-on-disk configuration (THT, Anton Paar TriTec) was used at room temperature, 200 °C, 400 °C and 600 °C. WC-6Co spheres of 3 mm diameter were used as counterparts at room temperature and 200 °C, to simulate the many applications where hardmetal coatings are typically coupled to other hardmetal coatings, e.g. in petrochemical ball valve applications (where both ball and seats are coated with hardmetal layers). Al_2O_3 spheres of the same diameter were employed at 400 °C and 600 °C, where WC-6%Co would not be usable because of excessive oxidation, to simulate the contact with a hard and chemically inert counterface. The test conditions were: a relative sliding speed of 0.4 m/s, a wear track radius of 7 mm, an overall sliding distance

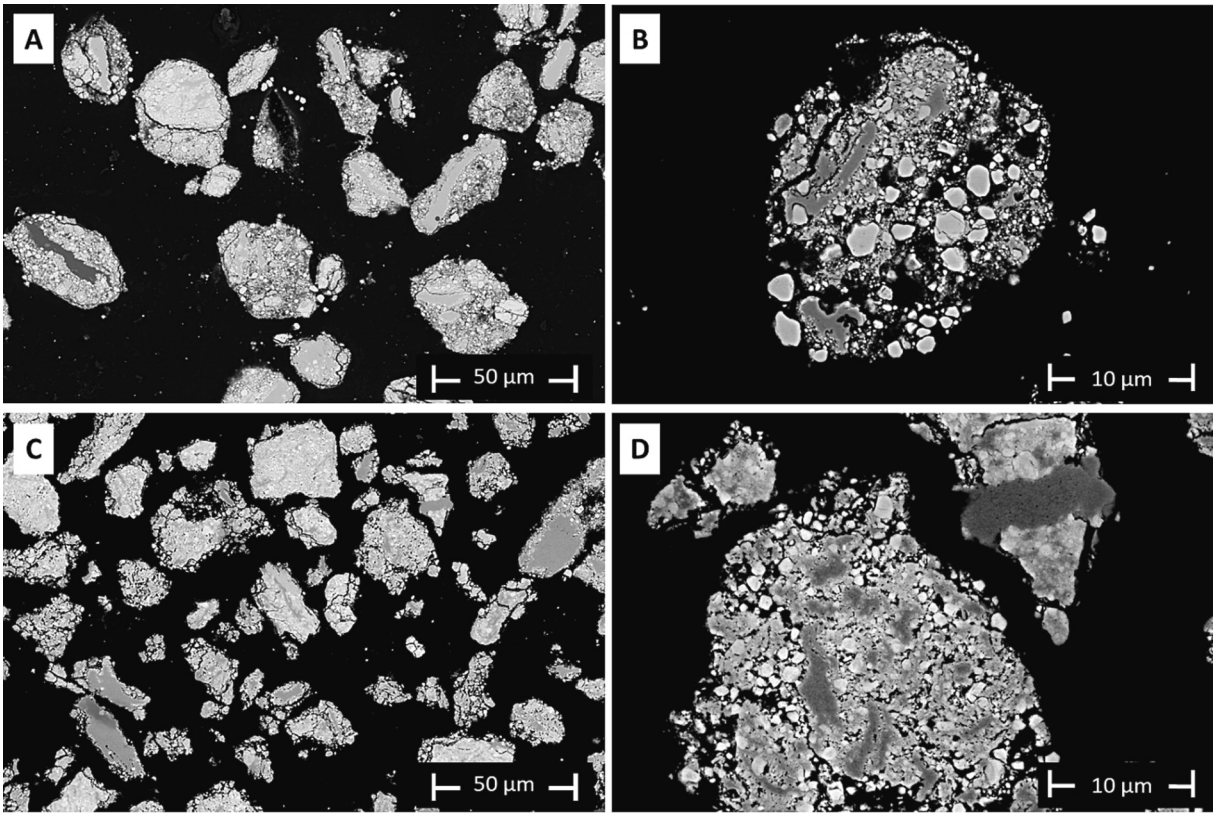

Fig. 1. SEM micrographs of the high-energy ball milled NbC-25NiCr (A, B) and NbC-40NiCr powders (C, D): overview (A, C) and high-magnification (B, D), respectively.

of 5000 m and a normal load of 10 N.

Assuming that the elastic moduli of the NbC-based coatings and the WC-6%Co balls are approximately 280 GPa (see the measured values in Section 3.3) and 620 GPa [36], the average and maximum Hertzian contact pressures at the beginning of the room-temperature tests under the given conditions are $p_{ave} \approx 2.3$ GPa and $p_{max} \approx 3.4$ GPa, with a subsurface shear stress maximum $\tau_{max} \approx 1.0$ GPa at a depth of around 18 µm (i.e. well within the coating). Because the elastic modulus of WC-6%Co changes only by approximately 10 GPa between room temperature and 200 °C [36], these estimates are approximately still valid for the tests at 200 °C.

Using the high-temperature data published by Wachtman and Lam [37], the elastic modulus of Al_2O_3 is 294 GPa at 400 °C and 286 GPa at 600 °C. Assuming as a reasonable guess that the elastic modulus of the NbC-based coatings decreases with temperature like that of a high-Co WC-Co composite [36], it can be tentatively estimated that the coatings' elastic moduli become 269 GPa at 400 °C and 262 GPa at 600 °C. Thus, the Hertzian contact pressures and shear stress maxima are $p_{ave} \approx 1.8$ GPa, $p_{max} \approx 2.7$ GPa, $\tau_{max} \approx 0.85$ GPa (depth: 20 µm) at both 400 °C and 600 °C (the decrease from 400 °C to 600 °C being marginal in the light of the highly approximate nature of these values). It is important to note that these values decrease rapidly during the test as the ball and the coated sample wear down and conform to each other.

In the ball-on-disc test, two samples for each coating type were used. The tangential force acting on the counterpart during the test was measured by a load cell and was used to monitor the coefficient of friction.

The wear rate of the samples was evaluated by volume loss, measured using the non-contact structured light profilometry technique (ConfoCam profilometer, Confovis GmbH, Jena, Germany, coupled to a Nikon Eclipse LV150N optical microscope). The wear rate of the counterparts was determined with the aid of an optical microscope, through which the diameter of the circular wear scar was measured.

After the dry sliding wear test, the morphology and chemical composition of surfaces and cross-sections of worn samples were determined by SEM + EDS. The cross-sections were prepared by cold-mounting the worn samples in epoxy resin before cutting them with a metallographic cutter to avoid damage and retain any surface layer. Then, they were ground and polished following the same methodology described in Section 2.2. The composition of the tribofilms formed within the wear track and the oxide scale formed outside the wear track of the NbC-NiCr coatings during tests carried out at 400 °C and 600 °C were studied using micro-Raman spectroscopy with a 532 nm-wavelength laser focused through a 100× objective (LabRam, Horiba Jobin-Yvon, Longjumeau, France).

2.4. Abrasion resistance

The abrasion resistance of the NbC-NiCr coatings and the reference coatings TiC-25NiCr, TiC-40NiCr, WC-CoCr, and Cr_3C_2-NiCr was determined by a dry particle abrasion test performed using FEPA-80 white alumina (≈185 µm average particle size). The test consisted of the alumina particles flowing approximately at a 100 g/min rate between the flat sample in a stationary position and a Fe360A steel wheel (200 mm diameter, 10 mm width) rotating at 85 rpm for 100 revolutions. The samples were pressed against the wheel by a normal load of 40.2 N. In total, 3 tests were carried out for each coating, and the samples were used in the as-deposited condition (not ground and polished).

The wear rate of the samples was evaluated by volume loss, measured using a focus-variation profilometry technique with the same ConfoCam profilometer described above. The morphology and chemical composition of the surfaces and cross-sections of the worn samples were assessed by SEM + EDS, following the same methodology described in Section 2.2.

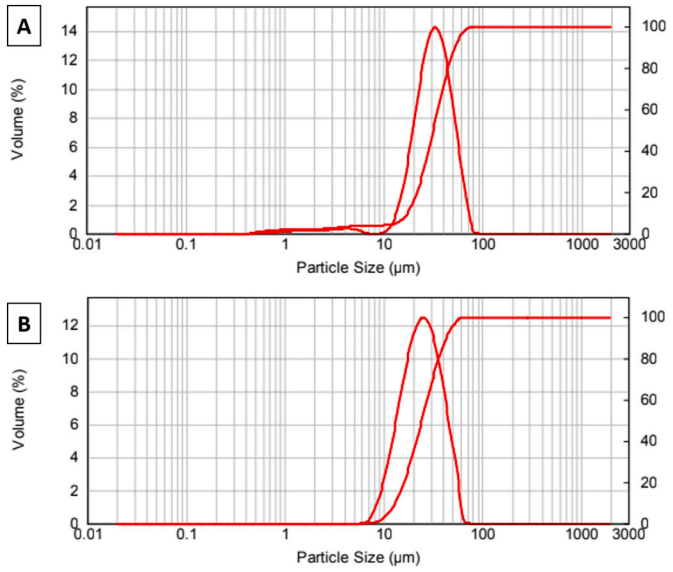

Fig. 2. Particle size distributions of the NbC-25NiCr (A) and NbC-40NiCr (B) feedstock powders.

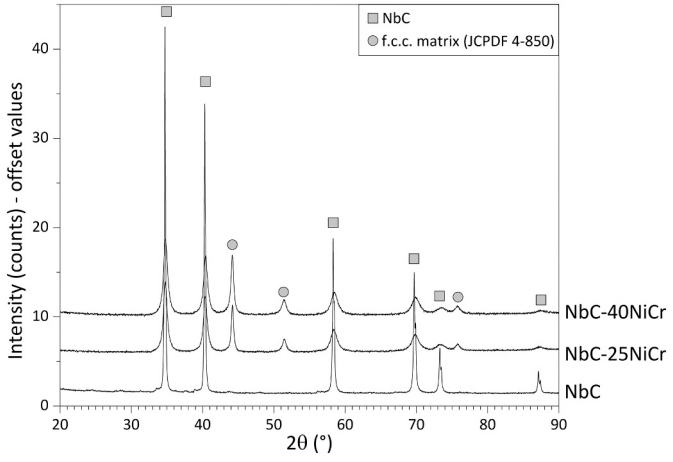

Fig. 3. XRD patterns of the NbC powder, NbC-25NiCr, and NbC-40NiCr feedstock powders.

2.5. Corrosion resistance

The corrosion resistance of NbC-NiCr coatings and WC-CoCr and Cr_3C_2-NiCr reference coatings was evaluated by electrochemical polarization testing in 3.5 % (wt./vol.) NaCl aqueous solution under aerated conditions at room temperature, using a three-electrode cell (K0235 flat cell: Ametek Princeton Applied Research) with a capacity of 300 mL, equipped with a Pt mesh counter-electrode and an $Ag/AgCl/KCl_{(sat.)}$ reference electrode. To maximize the impregnation of any open pores and stabilize the open circuit potential (OCP), the samples were left in contact with the test solution for 1 h before starting the potential scan. The conditions of the electrochemical polarization test were: an overpotential range of −400 mV/+1600 mV at a scan rate of 0.5 mV/s. Corrosion current density (I_{Corr}) and corrosion potential (E_{Corr}) were obtained by Tafel analysis according to the procedure previously described in [22]. After the electrochemical polarization test, the cross-sections of the corroded samples were analysed following the same cold-mounting epoxy resin assembly procedure described in Section 2.2.

3. Results and discussion

3.1. Structure, microstructure, and thermal properties of the powders

Powders manufactured by high-energy ball-milling (HEBM) can present irregular morphology or contain cracks caused by impact stress during the solid-state mechanical alloying process. Both characteristics mentioned above can be observed in the NbC-25NiCr and NbC-40NiCr powders (Fig. 1 A-D). However, the particles' morphology is still sufficiently rounded to be suitable for the HVOF thermal spray process [22]. According to Mahade et al. [38], a powder with a substantial surface-to-volume ratio would be undesirable for a thermal spray process as it would likely possess poor flowability along the feeding system. In the present case, however, particles with sufficiently rounded shape resulted in stable feed at the desired mass flow rate during the HVOF process. Analysing the images acquired at higher magnification (Fig. 1 B, D), we can note that the powder particles with NbC-25NiCr composition are less compact and less homogeneous compared to the NbC-40NiCr composition, which can be justified by the smaller amount of metallic phase available to bind the carbides. Additionally, it can be observed that the distribution of hard phase and matrix is not always homogeneous within a particle, despite the continuous process of repeated fracturing and welding that characterizes the HEBM process.

Fig. 2 A-B shows that the NbC-25NiCr powder is slightly coarser than the NbC-40NiCr powder. Their respective particle size distributions, characterized by $d_{10} = 17$ μm, $d_{50} = 32$ μm, $d_{90} = 52$ μm and $d_{10} = 13$ μm, $d_{50} = 24$ μm, $d_{90} = 43$ μm, confirm the nominal size distributions measured by MBN Nanomaterialia. A similar difference in particle size distribution was previously observed between TiC-25NiCr and TiC-40NiCr compositions, obtained by the same HEBM process [22]. Anyway, both niobium carbide (NbC)-based feedstock powders, just like the previous compositions based on titanium carbide (TiC), fall within the particle size range (≈ 10–40 μm) suitable for the HVOF process [39,40]. According to [40], larger powder particles can result in the retention of unmelted particles in the microstructure of the sprayed coating layer. On the other hand, very fine particles are usually degraded (e.g., by oxidation, severe decarburization, etc.) before their contact with the substrate.

Analysing the phase composition of the pure NbC powder and the feedstock powders through the XRD technique (Fig. 3), no impurities were found in detectable amounts, nor differences in the intensities or position of the diffraction peaks. In both NbC-NiCr compositions, the main phases are NbC and a face-centred cubic phase corresponding to the nickel-based solid solution matrix. Compared to the XRD pattern of the pure NbC powder, the diffraction peaks of the NbC phase in the patterns of the feedstock powders exhibit significant broadening, which reflects the reduced crystallite size and increased micro-strain levels due to the HEBM process.

The thermogravimetric analysis of the powders showed that the two compositions studied have similar oxidation behaviour, albeit with slight differences. The NbC-25NiCr (Fig. 4 A) and NbC-40NiCr (Fig. 4 B) compositions began oxidizing at ≈310 °C and ≈300 °C, respectively. In both cases, a first maximum on both the DTA and DTG curves occurs at around 400–420 °C, which most likely corresponds to the formation of a protective oxide scale. This interpretation is corroborated by a subsequent decrease in the reaction rate at slightly higher temperatures. In both cases, further increases in temperature cause the onset of new oxidation reactions with additional weight gains. For the NbC-25NiCr composition, mass gain peaks were observed in the DTG curve (corresponding to local DTA maxima) at ≈720 °C and 1040 °C. For the NbC-40NiCr one, mass gain peaks occurred at ≈550 °C and 990 °C.

3.2. Structure and microstructure of the coatings

Fig. 5 shows the cross-sectional micrographs of two NbC-25NiCr and two NbC-40NiCr coatings – each deposited with parameters sets R1 (A-

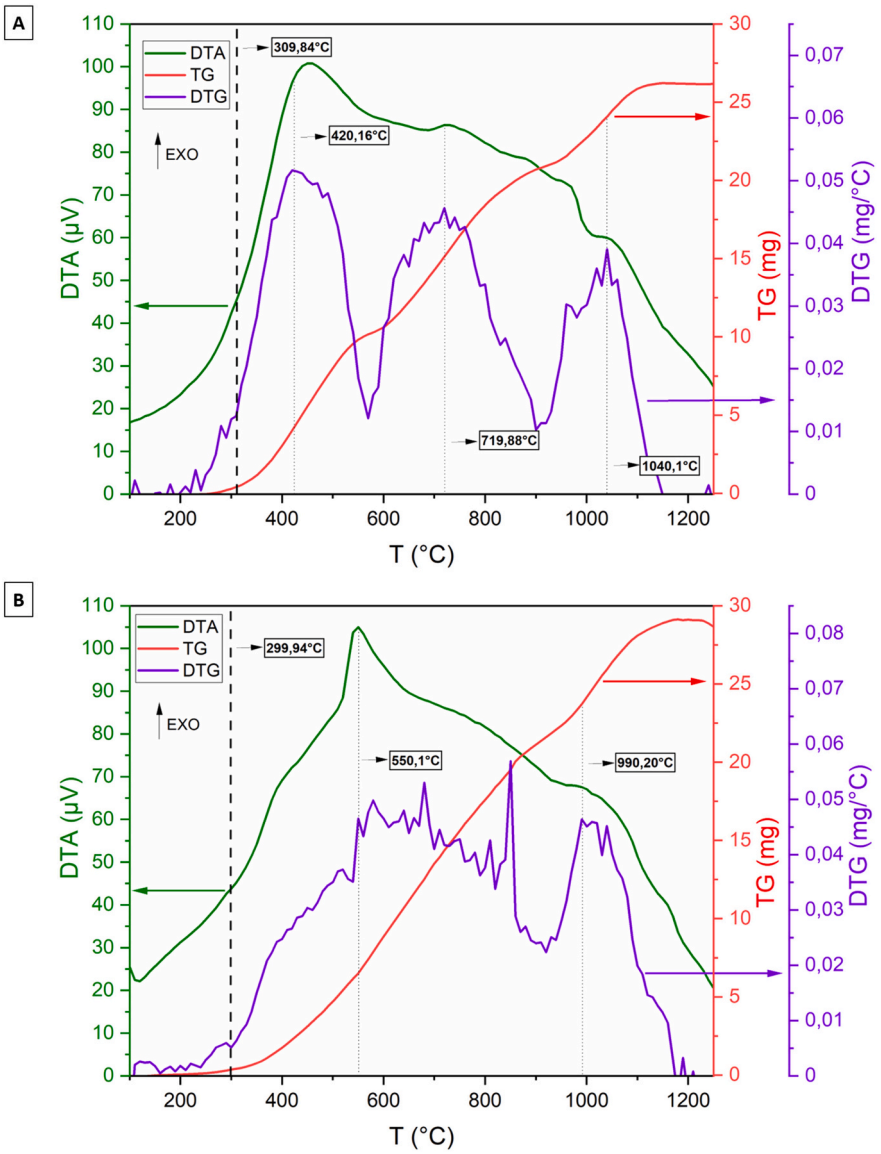

Fig. 4. Curves of TG/DTA/DTG obtained in the air for NbC-25NiCr (A) and NbC-40NiCr (B) feedstock powders.

C, G-I) and R2 (D—F, J-L) – while the corresponding values of deposition efficiency, thickness, and porosity are reported in Table 2. The latter contains these values also for the other NbC-40NiCr coatings deposited with parameter sets R3, R4 and R5.

It can be observed that, except for NbC-40NiCr – R1, which showed significantly lower porosity compared to the other samples, there are no significant variations among the microstructural characteristics of all the samples studied (porosity between 0.3 and 0.8 %). These results revealed that the NbC-based coatings could attain the typically low porosity expected of HVOF-sprayed hardmetals (< 1 %), and could be grown to a technologically useful thickness (> 200 µm) [41]. Furthermore, the NbC-25NiCr and NbC-40NiCr compositions are less porous compared to the TiC-NiCr coating compositions deposited previously [22,23], although their deposition efficiencies are lower than those attained with TiC-NiCr powders.

SEM micrographs acquired at intermediate and high magnifications (Fig. 5) show the presence of elongated oxide inclusions between the coating lamellae, as well as smaller rounded oxide inclusions within the lamellae. Oxide inclusions are a typical characteristic of HVOF coatings due to high-temperature oxidation of the particles either after deposition or during flight [42,43]. Some lamellae exhibit extensive inner oxidation. Just as we had previously discussed in the case of TiC-NiCr coatings, which exhibited similar forms of oxidation [22], it is possible to speculate that extensively oxidized lamellae (e.g. Fig. 5 F) might have originated from powder particles containing inner microcracks because of the HEBM process, as seen in Fig. 1. Cracks might have allowed oxidizing agents (including air entrained in the jet, as well as water vapour produced from the combustion) to penetrate to the interior of the particle itself. Occasionally, a lamella or a region within a lamella might show no distinguishable NbC particles (e.g. Fig. 5 F). This likely originated from the inhomogeneities previously seen in the feedstock powder (Section 3.1 and Fig. 1), where a few areas within a particle might not embed any NbC.

The XRD patterns comparing the NbC-25NiCr and NbC-40NiCr coatings (Fig. 6 A-B) show that the NbC phase remains predominant after deposition. The peaks of the matrix phase are notably displaced to lower diffraction angles, which indicates an increase in lattice spacing that is probably a consequence of the dissolution of some Nb and/or C during spraying. Other peaks of lower intensity indicate the presence of oxides formed during HVOF spraying.

Despite limitations in the quantification of light elements and the possibility of overestimating their content, the EDX technique (results

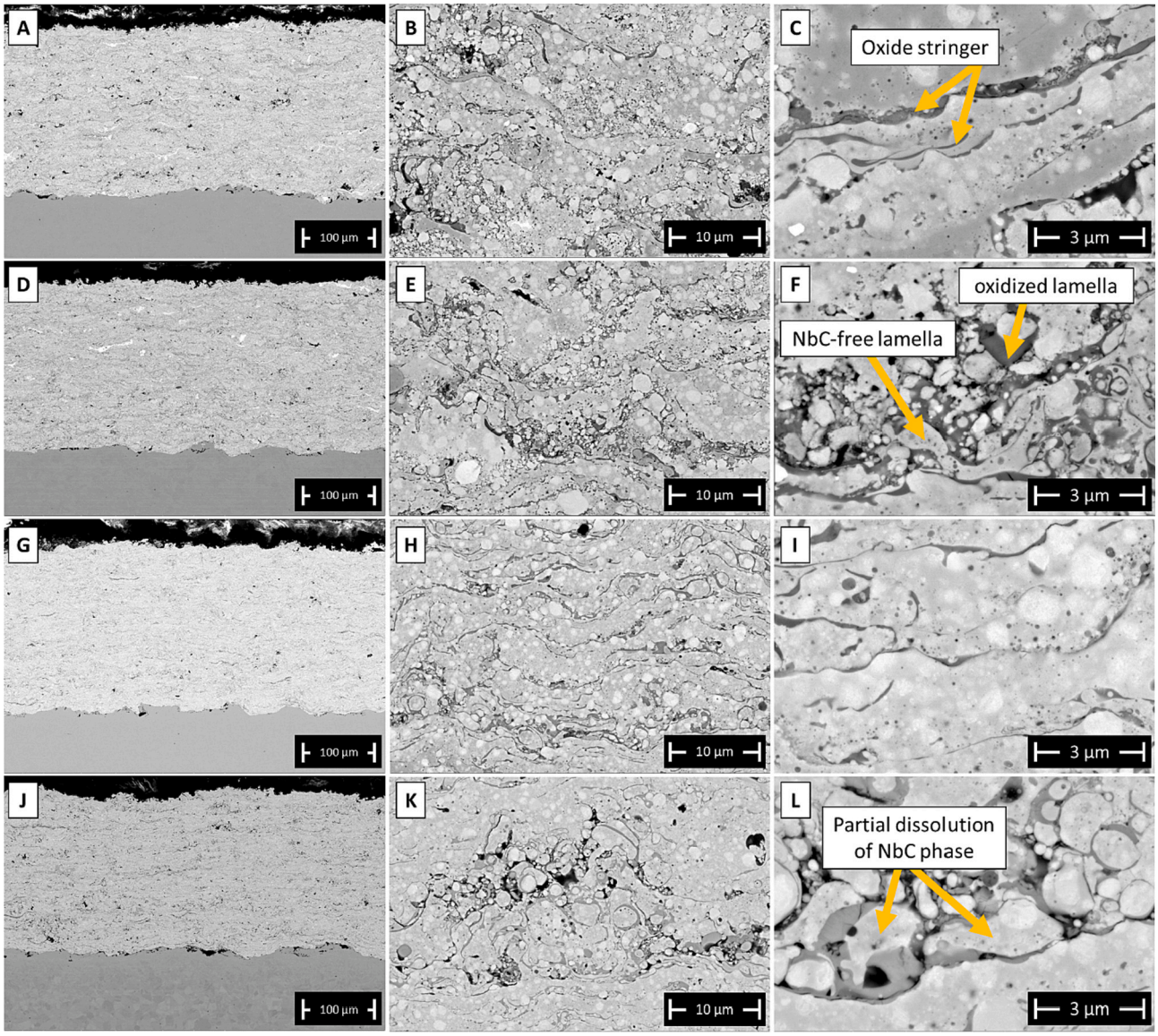

Fig. 5. SEM micrographs of the cross-section of the HVOF-sprayed coatings NbC-25NiCr (A-F) and NbC-40NiCr (G-L), deposited using the set of process parameters R1 (A-C, G-I) and R2 (D—F, J-L): low magnification overviews (A, D, G, J), intermediate (B, E, H, K) and high-magnification (C, F, I, L) details.

Table 2
Deposition efficiency (%), thickness (µm), and porosity (%) of NbC-25NiCr and NbC-40NiCr coatings.

	Set	Deposition efficiency (%)	Thickness (µm)	Porosity (%)
NbC-25NiCr	R1	48.6	234 ± 11	0.46 ± 0.14
	R2	48.4	228 ± 6	0.30 ± 0.09
NbC-40NiCr	R1	46.4	225 ± 7	0.06 ± 0.06
	R2	45.6	213 ± 7	0.81 ± 0.13
	R3	45.6	217 ± 7	0.63 ± 0.05
	R4	47.6	226 ± 8	0.77 ± 0.17
	R5	48.1	245 ± 7	0.61 ± 0.06

shown in Table 3) revealed a significant uptake of oxygen (≈ 4–5 %) in both types of coatings after thermal spraying, compared to the feedstock powders (≈1 wt%). The coatings also exhibited a reduction in the content of Nb, compared to the amount detected in the powders. In contrast, an increase in the content of matrix elements (Ni and Cr) was detected. This might reflect selective rebounding of carbide-rich powder particles, due to their poorer deformability, resulting in a loss of Nb in the coatings. Such preferential rebounding of carbide-rich particles is known e.g. for Cr_3C_2-NiCr coatings [44]. This change in elemental composition before and after deposition was not noted with TiC-NiCr coatings, which might be due to the higher density (hence, higher momentum and kinetic energy at impact) of NbC-containing materials compared to TiC-based ones (for a given volume fraction of hard phase). On the other hand, the denser NbC-NiCr particles might exert a stronger peening action on the previously deposited material, compared to TiC-NiCr ones. This could explain the slightly lower porosity of NbC-NiCr coatings compared to TiC-NiCr ones with nominally identical volumetric composition. A corresponding change in the carbon content, which is expected in case of carbide loss, was not seen in Table 3 probably because of the mentioned poor accuracy of EDX with light elements.

Powders and coatings also contain trace amounts of impurities (Fe, Ti, Si, W) possibly coming from the raw materials and/or the milling media. The slightly higher amount of Si measured in the powders (Table 3) is likely just an artefact due to the retention of some colloidal silica particles (from the final polishing stage, see Section 2.2) on the surface of the epoxy resin mount.

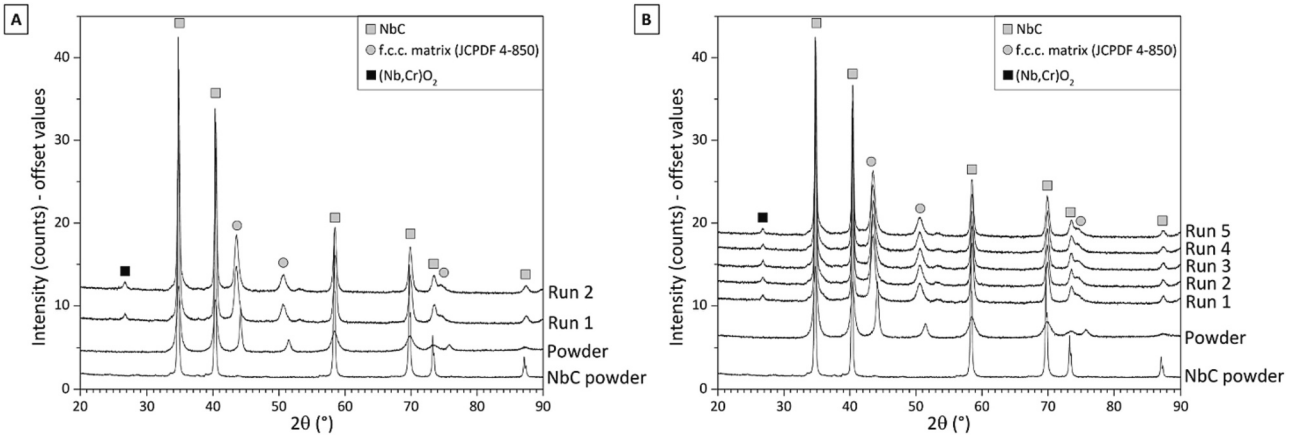

Fig. 6. XRD patterns of NbC-25NiCr (A) and NbC-40NiCr (B): comparison among pure NbC powder, feedstock powders, and their corresponding coatings.

Table 3
Quantitative EDX analyses (in weight %) of NbC-25NiCr and NbC-40NiCr (feedstock powders and coatings): average ± error range.

		Nb	Ni	Cr	Fe	Ti	Si	W	C	O
NbC-25NiCr	Nominal[a]	65.8	21.0	5.2	–	–	–	–	8.0	–
	Powder	66.81 ± 0.71	18.87 ± 0.46	4.77 ± 0.22	0.09 ± 0.09	0.17 ± 0.10	1.42 ± 0.18	0.08 ± 0.08	6.93 ± 0.07*	1.50 ± 0.01**
	R1	53.77 ± 0.39	25.91 ± 0.12	5.85 ± 0.02	0.44 ± 0.02	0.17 ± 0.04	0.27 ± 0.02	0.33 ± 0.04	8.43 ± 0.53	4.82 ± 0.02
	R2	53.70 ± 0.06	26.71 ± 0.39	5.85 ± 0.05	0.50 ± 0.07	0.20 ± 0.03	0.24 ± 0.01	0.32 ± 0.05	7.49 ± 0.23	4.99 ± 0.17
NbC-40NiCr	Nominal[a]	52.2	33.2	8.3	–	–	–	–	6.2	–
	Powder	55.00 ± 0.47	29.69 ± 0.35	7.73 ± 0.14	0.14 ± 0.06	0.38 ± 0.09	0.51 ± 0.03	0.12 ± 0.03	6.03 ± 0.02*	0.86 ± 0.01**
	R1	47.80 ± 0.23	33.15 ± 0.32	7.31 ± 0.08	0.34 ± 0.01	0.30 ± 0.03	0.18 ± 0.01	0.11 ± 0.08	6.44 ± 0.21	4.37 ± 0.07
	R2	47.00 ± 0.33	33.19 ± 0.13	7.20 ± 0.09	0.28 ± 0.05	0.34 ± 0.05	0.29 ± 0.04	0.11 ± 0.05	6.98 ± 0.27	4.62 ± 0.13
	R3	47.30 ± 0.23	33.28 ± 0.34	7.39 ± 0.06	0.28 ± 0.06	0.34 ± 0.03	0.30 ± 0.03	0.17 ± 0.08	6.51 ± 0.13	4.43 ± 0.22
	R4	47.69 ± 0.23	33.23 ± 0.27	7.30 ± 0.08	0.31 ± 0.01	0.39 ± 0.06	0.27 ± 0.03	0.12 ± 0.07	6.56 ± 0.10	4.14 ± 0.03
	R5	47.62 ± 0.14	32.03 ± 0.40	7.37 ± 0.06	0.31 ± 0.03	0.35 ± 0.04	0.32 ± 0.02	0.16 ± 0.07	7.00 ± 0.17	4.84 ± 0.11

* Value by the inert gas fusion method.
** Value by the oxygen combustion method.
[a] The nominal chemical composition of the feedstock material powders was provided by MBN Nanomaterialia.

Table 4
Elastic modulus and Vickers microhardness of NbC-25NiCr, NbC-40NiCr, and WC-CoCr coatings. Reference values for TiC-25NiCr and TiC-40NiCr are taken from our previous publication [22].

Coating material	Set	E_{IT} (GPa)	$HV_{0.3}$
NbC-25NiCr	R1	279 ± 17	864 ± 82
	R2	285 ± 13	928 ± 69
NbC-40NiCr	R1	282 ± 12	1034 ± 82
	R2	327 ± 16	990 ± 106
	R3	269 ± 17	966 ± 101
	R4	278 ± 13	968 ± 104
	R5	275 ± 11	978 ± 83
WC-CoCr	–	393 ± 38	1473 ± 255
TiC-25NiCr [22]	–	160 ± 7	791 ± 79
TiC-40NiCr [22]	–	155 ± 5	838 ± 66

3.3. Microindentation testing

Considering the associated error ranges, the NbC-25NiCr and NbC-40NiCr coatings have microhardness values of ≈900 $HV_{0.3}$ and ≈1000 $HV_{0.3}$ (respectively), mostly independent of the deposition conditions (Table 4). Elastic moduli are around ≈280 GPa in all cases. Although these hardness values are lower than the conventional WC-CoCr reference coating, they are slightly higher than those measured for the TiC-NiCr coatings (reproduced in Table 4 from our previous work [22]) and comparable to or slightly higher than the values listed by different literature sources for HVOF-sprayed Cr_3C_2-NiCr (WOKA 7102) [23,45], which were measured under the same test conditions.

The lower hardness of the NbC-25NiCr compositions compared to NbC-40NiCr compositions, despite the higher NbC content, can be explained by a certain brittleness of the former coatings. In Fig. 7, the cross-sectional micrograph of NbC-25NiCr-R2 presents a Vickers indentation mark, where some microcracks are visible. Cracking facilitates the inelastic deformation of the sample during the indentation test, resulting in lower measured hardness. A similar behaviour was previously observed when comparing TiC-25NiCr and TiC-40NiCr compositions, as reflected by the corresponding data listed in Table 4 [22]. The slightly higher average hardness of NbC-40NiCr-R1 coating (≈ 1034 $HV_{0.3}$) compared to the other NbC-based samples is correlated with the

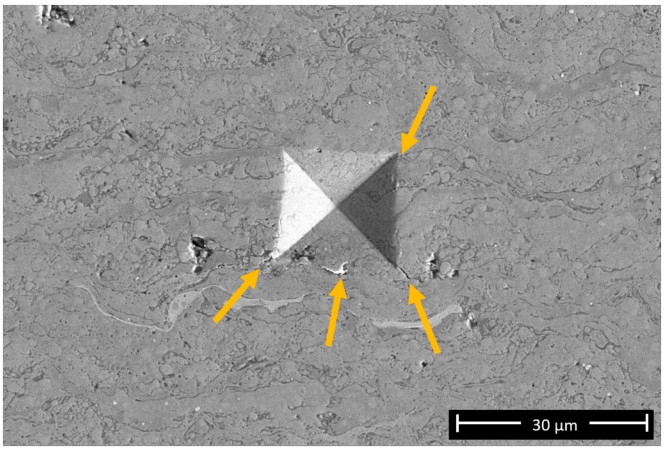

Fig. 7. SEM micrograph of the cross-section of the NbC-25NiCr set R2 coating, highlighting a Vickers indentation mark. Arrows indicate microcracks.

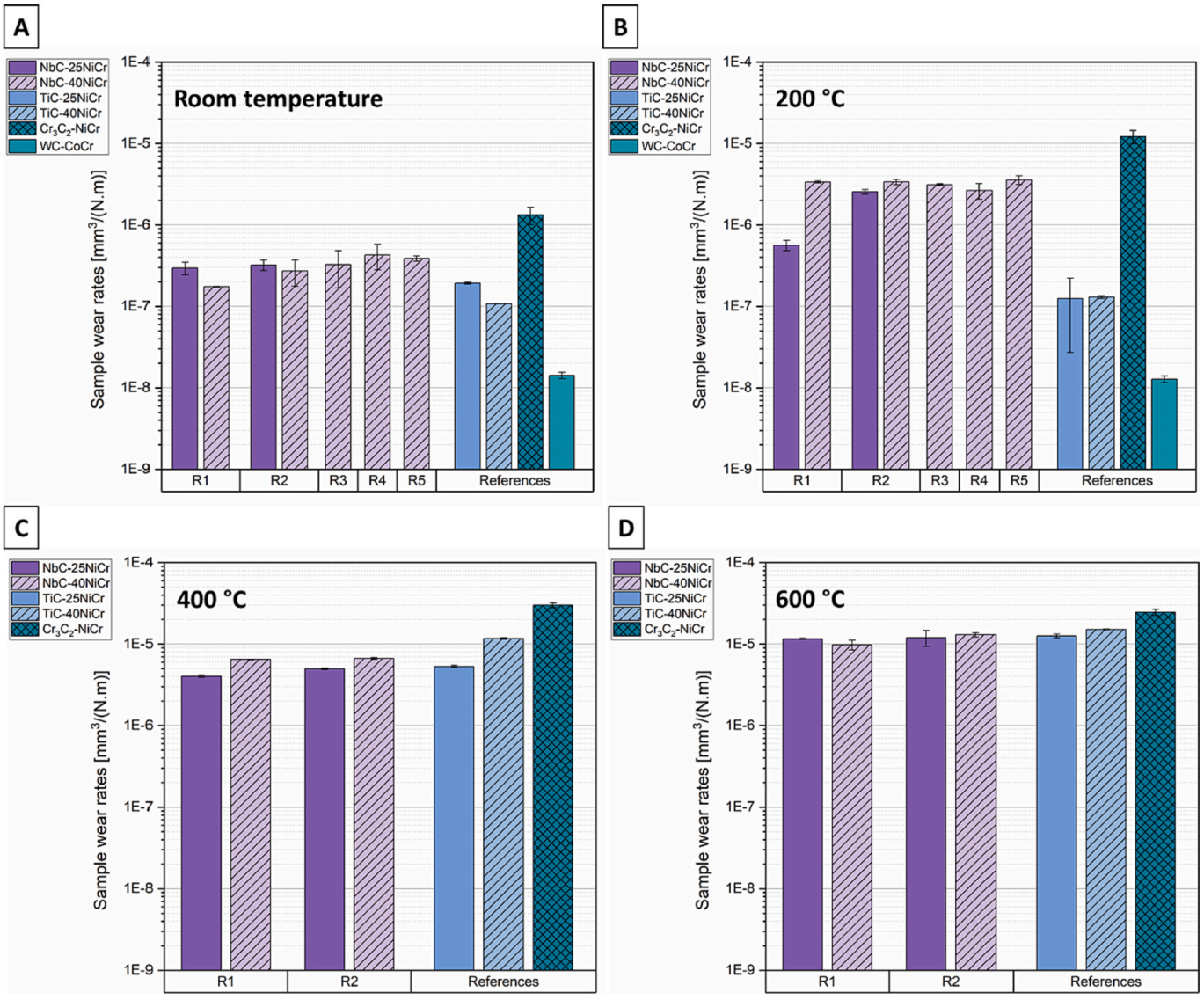

Fig. 8. Ball-on-disk dry sliding wear rates of all samples, measured at room temperature (A), 200 °C (B), 400 °C (C) and 600 °C (D) using WC-6Co (RT and 200 °C) and Al_2O_3 (400 and 600 °C) balls of 3 mm-diameter, 0.4 m/s speed, and 10 N load.

lower porosity presented by this sample. Porosity and microhardness have a direct correlation since pores are weak points that might degrade the mechanical strength of a material [46,47].

3.4. Sliding wear resistance

3.4.1. Dry sliding wear resistance at room temperature

For all NbC-25NiCr and NbC-40NiCr coatings similar wear rates in the range of 2–4 $\times$ 10^{-7} $mm^3/(N{\cdot}m)$ were measured, under the ball-on-disc test conditions described in Section 2.3. Notably, the NbC-40NiCr-R1 sample, with slightly higher hardness and lower porosity, also exhibits the lowest wear rate [$\approx$2 $\times$ 10^{-7} $mm^3/(N{\cdot}m)$]. However, the difference is barely significant in light of the error ranges and the typical scatter associated with tribological tests [48]. These values are also within the same order of magnitude as those observed for TiC-25NiCr [2 $\times$ 10^{-7} $mm^3/(N{\cdot}m)$] and TiC-40NiCr [1 $\times$ 10^{-7} $mm^3/(N{\cdot}m)$] reference coatings. They are intermediate between conventional WC-CoCr and Cr_3C_2-NiCr coatings, whose wear rates, under the present test conditions, are 1 $\times$ 10^{-8} $mm^3/(N{\cdot}m)$ and 1 $\times$ 10^{-6} $mm^3/(N{\cdot}m)$, respectively. Interestingly, in our previous work [22], the same TiC-25NiCr and TiC-40NiCr coatings exhibited very similar specific wear rates when subjected to different ball-on-disc test conditions (most importantly, with a 6-mm Al_2O_3 ball as a counterpart instead of 3-mm WC-6%Co). It might suggest a certain stability of the specific wear rates when these materials are slid against a hard counterface, irrespective of the specific composition of such counterface.

Fig. 10 A shows that the specific wear rates of the counterparts are consistently lower than those of the corresponding coatings except for the counterpart used in contact with the Cr_3C_2-NiCr sample. The latter suffered a wear rate as high as that of the corresponding coating and, therefore, much higher than the specific wear rates of the WC-6%Co balls used against the other coatings. It suggests that not only is Cr_3C_2-NiCr less resistant to sliding wear against the hard WC-6Co counterpart, but it also causes more damage to this counterpart, perhaps due to the release of a large amount of abrasive wear debris. It would be consistent with the extensive abrasive grooving seen in the optical micrograph of the WC-6%Co ball tested against Cr_3C_2-NiCr (Fig. 10 B). Conversely, the NbC-40NiCr coatings (with the partial exception of the R3 sample) caused less wear damage to the counterface than the TiC-NiCr and Cr_3C_2-NiCr coatings did. The wear rate of the counterpart is, in this case, equivalent to that caused by the WC-CoCr coating.

NbC-25NiCr and NbC-40NiCr coatings produced friction coefficient

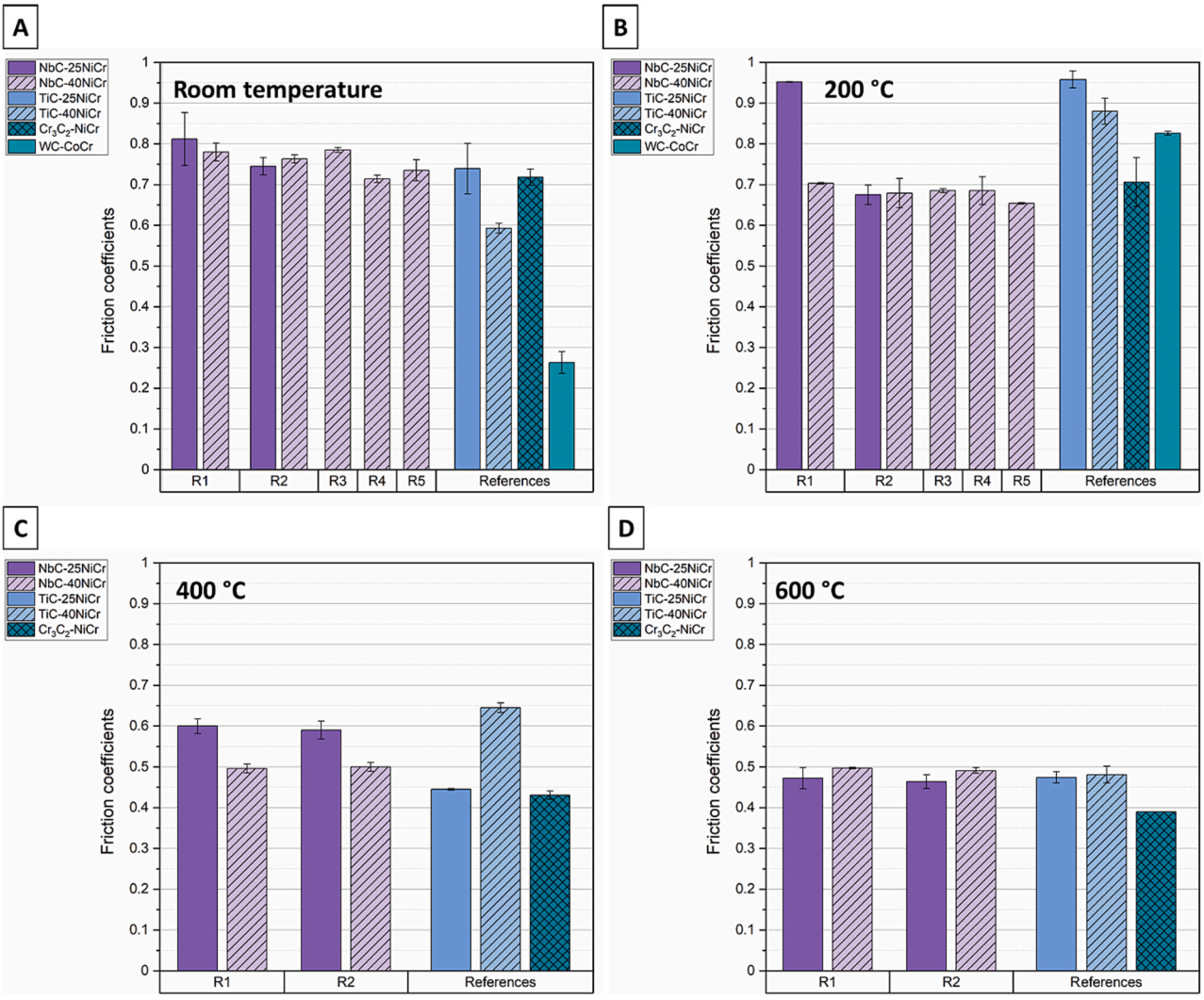

Fig. 9. Average friction coefficients of all samples, measured at room temperature (A), 200 °C (B), 400 °C (C) and 600 °C (D) using WC-6Co (RT and 200 °C) and Al_2O_3 (400 and 600 °C) balls of 3 mm-diameter, 0.4 m/s speed, and 10 N load.

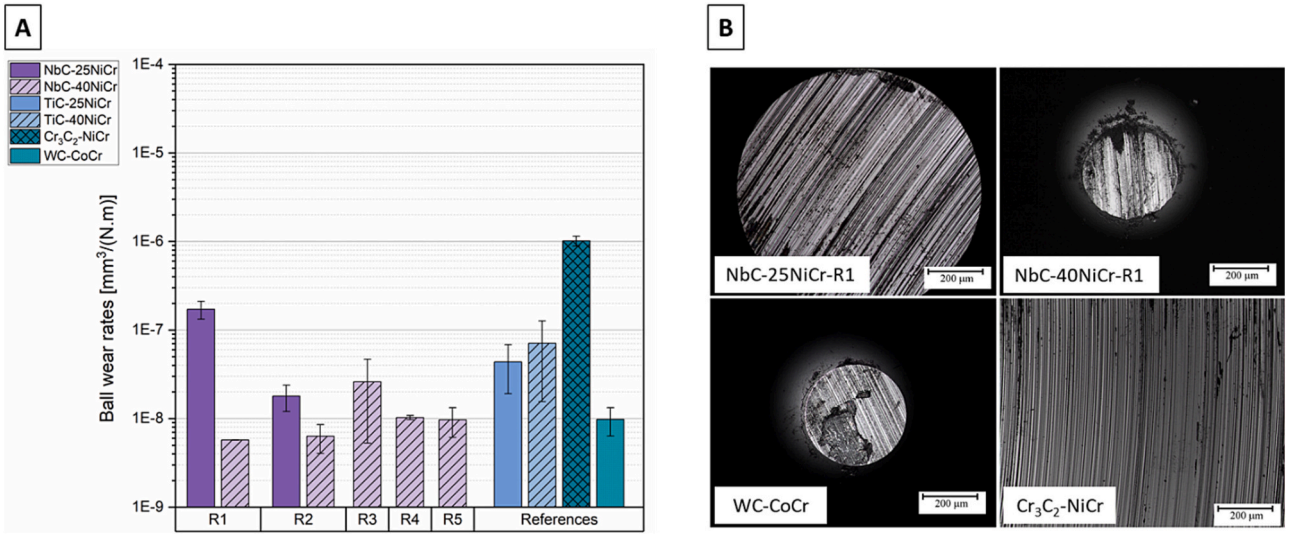

Fig. 10. Wear rates (A) and optical micrographs of the wear tracks (B) on the WC-6Co counterparts after ball-on-disc sliding wear tests at room temperature.

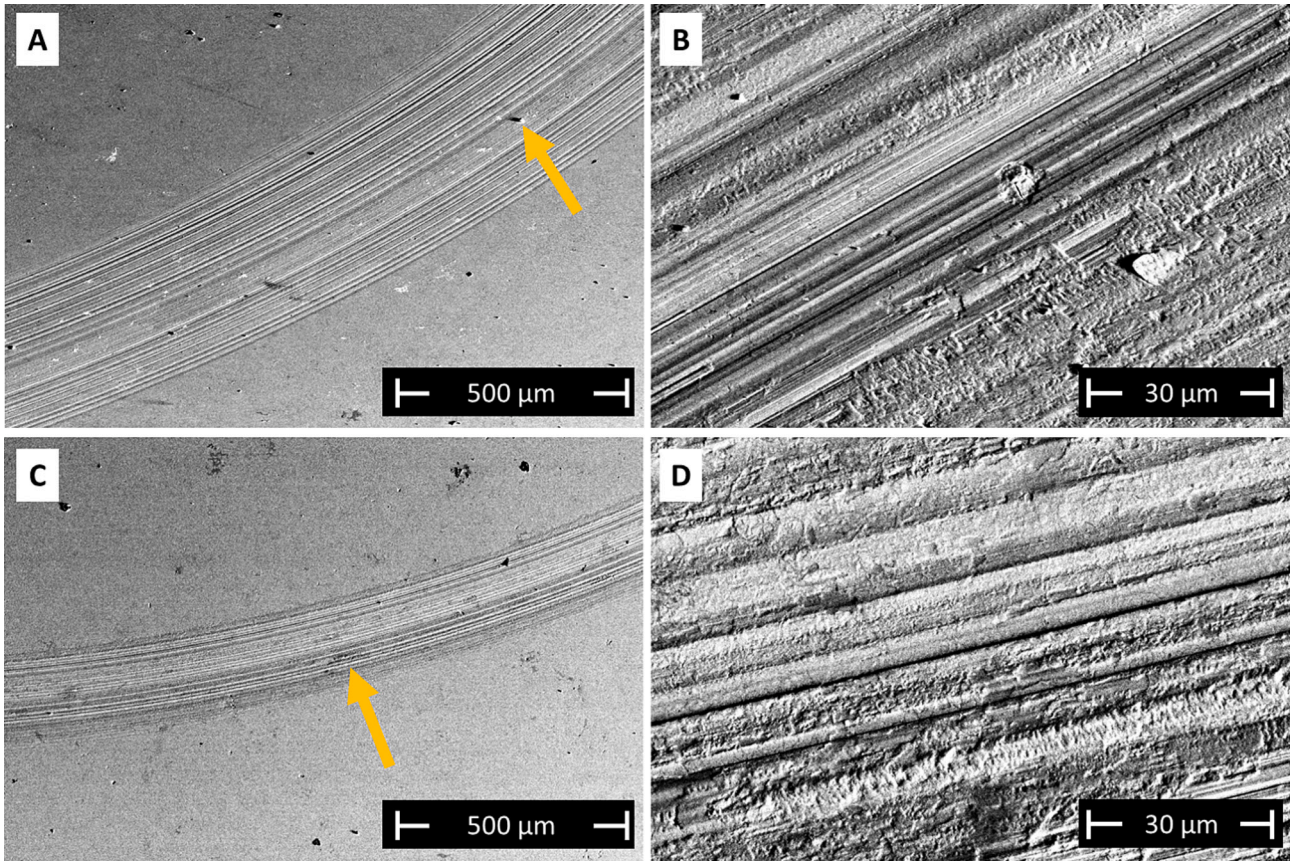

Fig. 11. SEM micrographs of ball-on-disk wear tracks on the NbC-25NiCr set R1 (A, B) and NbC-40NiCr set R1 (C, D) coatings after room temperature tests: overviews, with arrows indicating abrasive grooves (A, C), and details (B, D).

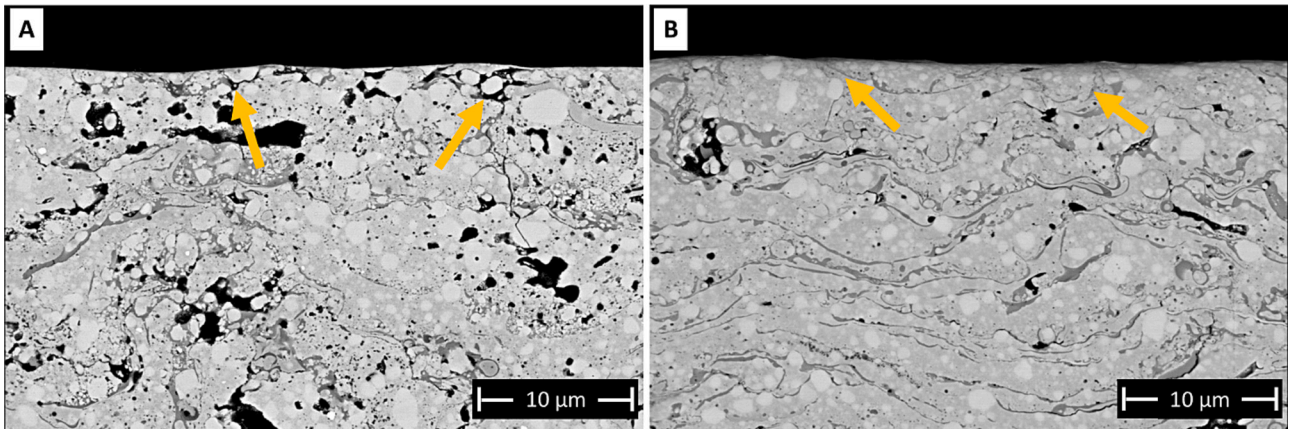

Fig. 12. SEM micrographs of the cross-section of the wear tracks produced on the NbC-25NiCr set R1 (A) and NbC-40NiCr set R1 (B) coatings after room temperature tests. Arrows indicate microcracks.

values in the same range (≈ 0.7–0.8 for every sample), similar to (or slightly higher than) those produced by the TiC-25NiCr and Cr_3C_2-NiCr coatings (Fig. 9 A). On the other hand, the WC-CoCr coating produced the lowest friction coefficient values in these tests (≈ 0.3), despite the chemical compatibility between the coating itself and the WC-6%Co counterpart. It suggests that the chemical inertness of the WC hard phase, and the high hardness of the coating effectively prevented any significant adhesion phenomenon. On the other hand, it is possible to speculate that an abrasive contribution to friction [49] caused the higher values seen in the tests with NbC-, TiC- and Cr_3C_2-based coatings.

Accordingly, the SEM images obtained from the surfaces of the NbC-25NiCr-R1 (Fig. 11 A-B) and NbC-40NiCr-R1 (Fig. 11 C—D) coatings after the wear process at room temperature show grooves produced by the asperities of the counterpart or by wear debris particles released by the mating bodies. Moreover, the slight difference between the wear rate of the NbC-40NiCr R1 coating and the other NbC-based coatings is reflected by morphological differences between the micrographs of the respective wear tracks. For instance, the NbC-25NiCr-R1 coating shows a larger wear track with deeper abrasive grooves compared to the NbC-40NiCr-R1 coating, and the cross-sections of the wear tracks (Fig. 12 A-B) also display a few more sub-surface pores and a few more microcracks in the NbC-25NiCr coating.

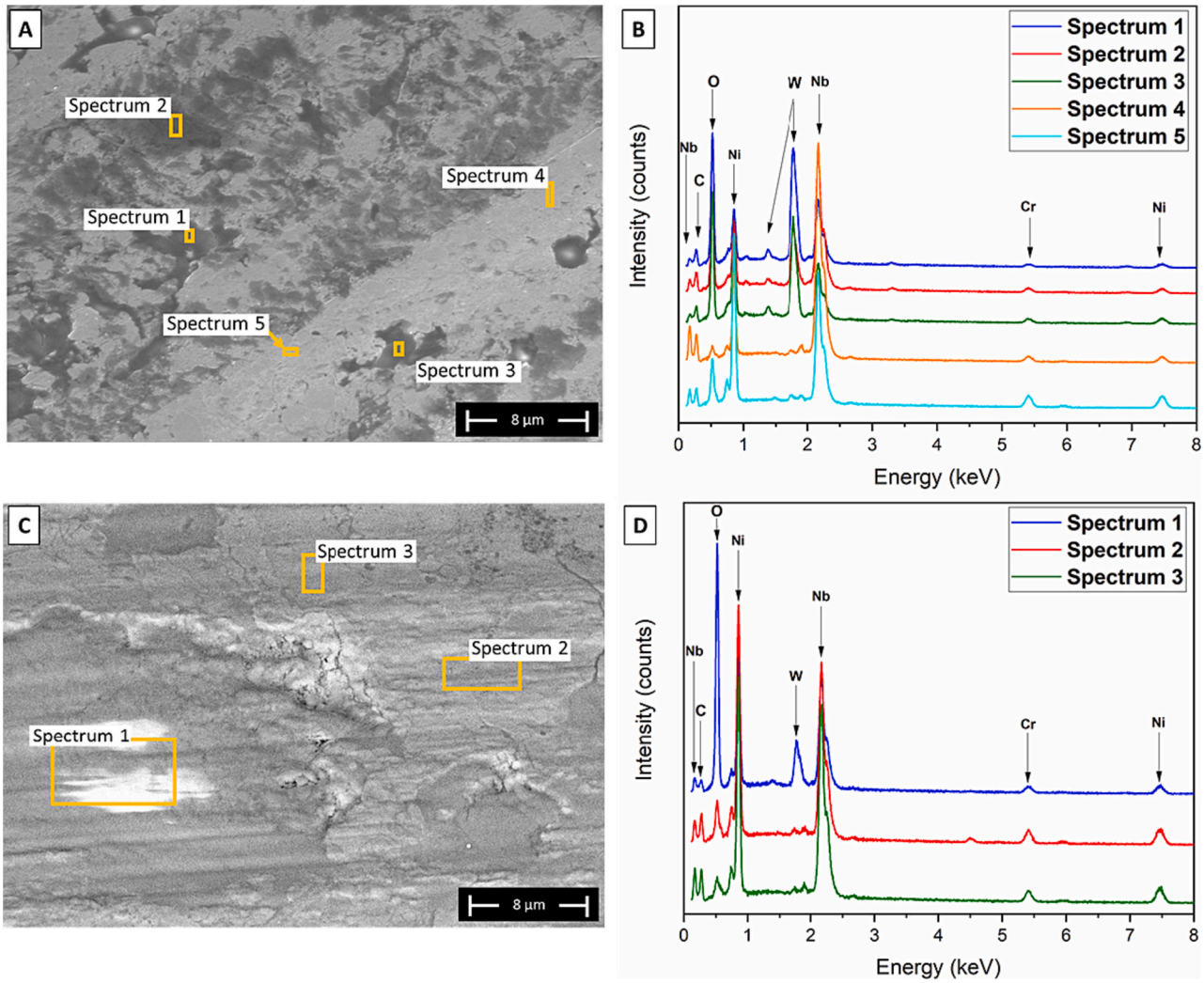

Fig. 13. SEM micrographs of inner zones of the ball-on-disk wear tracks on the NbC-25NiCr set R1 (A) and NbC-40NiCr set R1 (C) coatings after room temperature tests, and their corresponding EDX spectra (B, D).

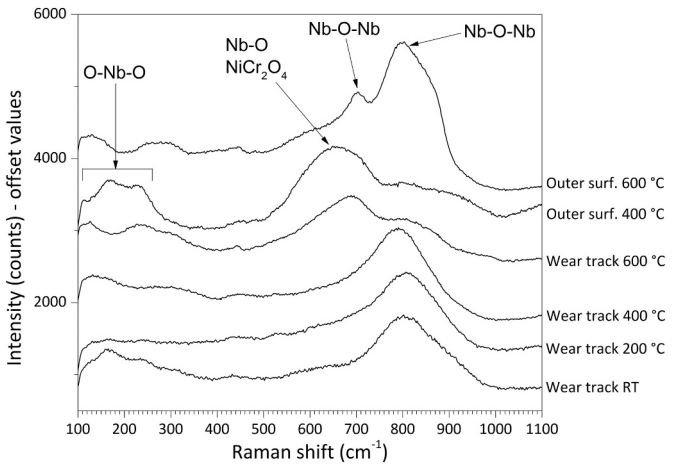

Fig. 14. Micro-Raman spectra acquired on oxidized patches within the wear tracks on the NbC-40NiCr coatings at all test temperatures, and outside the wear tracks after the tests at 400 °C and 600 °C.

The EDX analysis (Fig. 13 A-D) carried out at higher magnifications in the debris patches visible within the worn areas revealed the presence of tungsten and oxygen in addition to niobium, chromium, and nickel (i.e., the elements that make up the coating itself). Tungsten reflects the presence of debris coming from the wear of the counterpart (WC-6Co). In contrast, the presence of oxygen in the contact zone can be explained by tribo-oxidation of the debris. Namely, the debris patches on the worn surface consist of tribo-oxidized particles released by the coating itself and, to a lower extent, by the counterpart.

Accordingly, the typical Raman spectrum of these oxidized patches (Fig. 14), characterized by a broad band centred roughly around 800 cm^{-1}, is indicative of a poorly crystalline form of columbite-type Nb oxides, the band being ascribable to Nb-O-Nb bending in NbO_6 octahedra [50,51], although anhydrous WO_3 might also be contributing [52].

Tribo-oxidative formation of niobium-based oxides has also been reported for bulk NbC-based hardmetals [53], and it was found to play a significant role in the tribological response under dry sliding conditions, since the trends in both friction and specific wear rates of NbC-based hardmetals and sintered Nb_2O_5 as a function of temperature and sliding speed were found to be identical. Notably, even NbC-based hardmetals and sintered Nb_2O_5 exhibited rather high friction coefficients (>0.7) under unidirectional dry sliding at room temperature when the relative linear velocity was around 0.2 m/s, as in the present

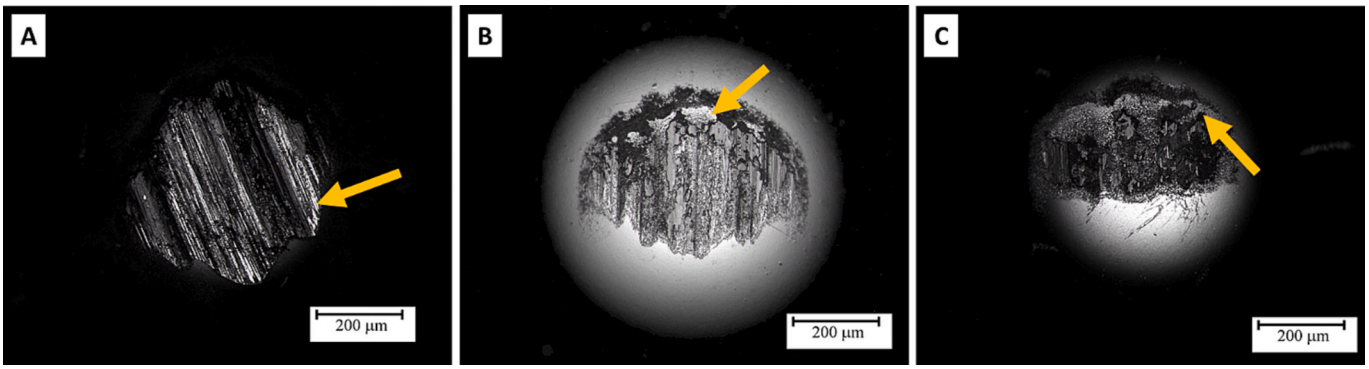

Fig. 15. Optical micrographs of the wear tracks on the WC-6Co counterparts after ball-on-disc sliding wear test at 200 °C against the NbC-25NiCr set R1 (A), NbC-25NiCr set R2 (B), and NbC-40NiCr set R1 (C) coatings. Arrows indicate abrasive grooves and the possible adhesive transfer of the coating to the counterparts.

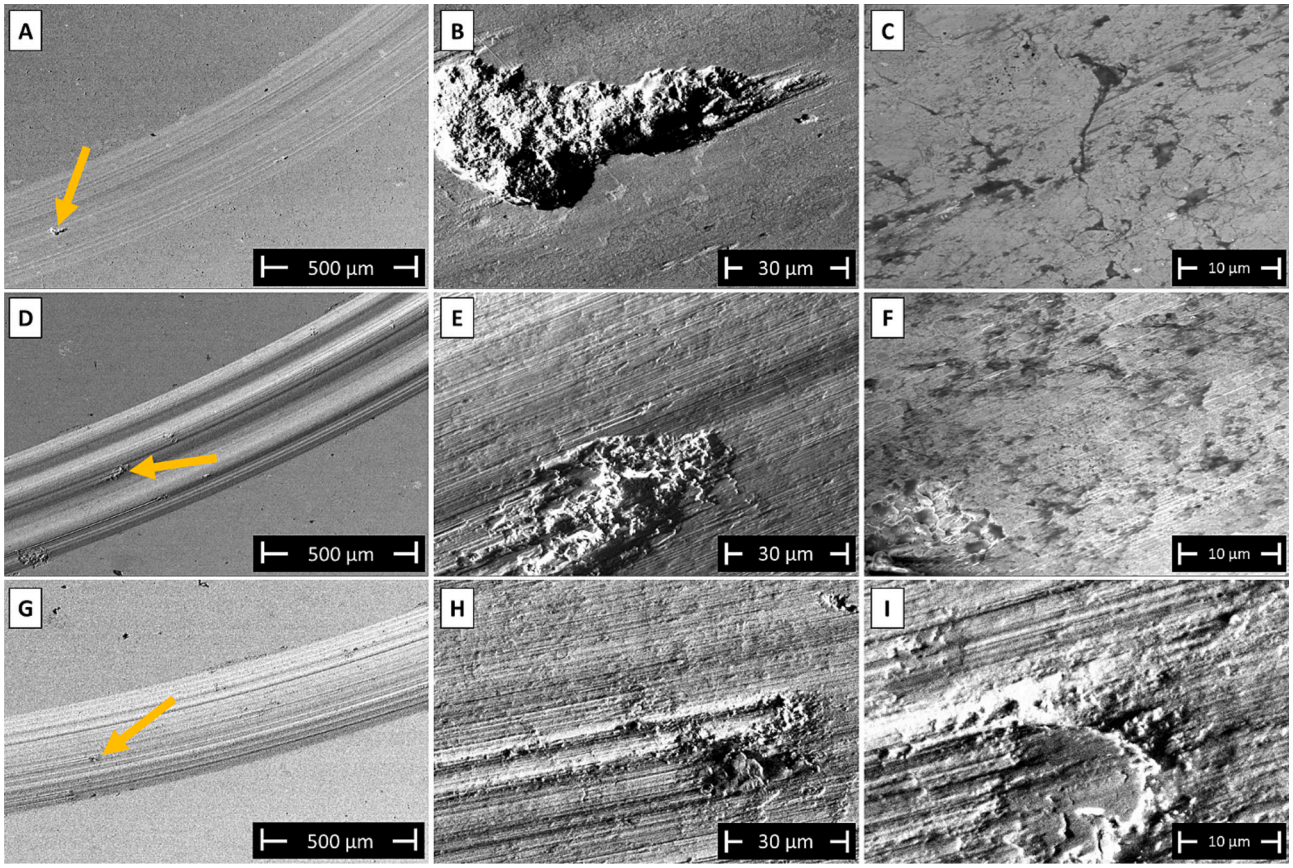

Fig. 16. SEM micrographs of ball-on-disk wear tracks on the NbC-25NiCr set R1 (A-C), NbC-25NiCr set R2 (D—F), and NbC-40NiCr set R1 (G-I) coatings after tests at 200 °C: overviews, with arrows indicating adhesive wear (A, D, G) and details at intermediate magnification (B, E, H) and high magnification (C, F, I).

case [53,54]. Lower friction was reportedly produced at much higher linear velocities, which are out of the scope of this work.

3.4.2. *Dry sliding wear resistance at 200 °C*

Except for the NbC-25NiCr-R1 sample, which displayed a lower wear rate of approximately 6×10^{-7} mm^3/(N·m), at 200 °C the average wear rates of NbC-25NiCr and NbC- 40NiCr coatings fall in the range of ≈ 3–4 $\times 10^{-6}$ mm^3/(N·m) (Fig. 8 B). These rates are significantly higher than those produced by the titanium carbide-based reference coatings, ≈ 1×10^{-7} mm^3/(N·m), and the WC-CoCr coating, 1×10^{-8} mm^3/(N·m). However, NbC-25NiCr and NbC-40NiCr samples exhibit higher wear resistance than the conventional Cr_3C_2-NiCr coating, whose specific wear rate is around 1×10^{-5} mm^3/(N·m).

In contrast to its wear resistance, the NbC-25NiCr-R1 sample produces a higher friction coefficient (≈ 1) compared to other coatings based on NbC and Cr_3C_2-NiCr, which produced an average coefficient of friction of ≈0.7 under the present test conditions (Fig. 9 B). Optical micrographs show the formation of an extensive layer of transferred material on the WC-6Co counterface, part of which seems to be not fully oxidized, based on its metallic shine, indicating an adhesive wear component consistent with relatively high friction.

However, unlike what was observed at room temperature, at 200 °C the TiC-25NiCr, TiC-40NiCr, and WC-CoCr reference coatings produced even higher mean friction coefficients (≈ 0.8–1) than most NbC-based samples.

From the optical micrographs in Fig. 15 A-C, it is also noted that the

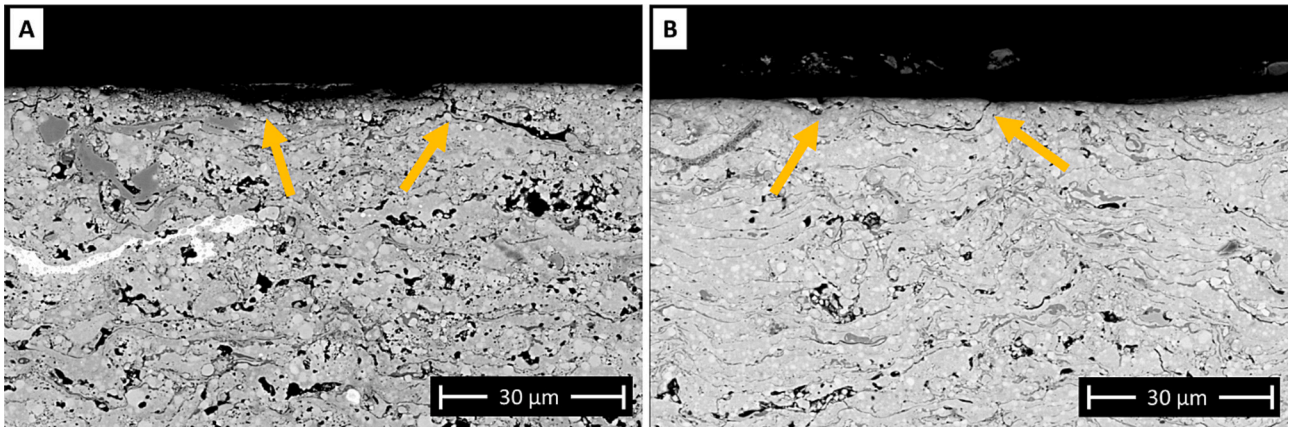

Fig. 17. SEM micrographs of the cross-section of the wear tracks on the NbC-25NiCr set R1 (A) and NbC-40NiCr set R1 (B) coatings after tests at 200 °C. Arrows indicate sub-surface microcracks.

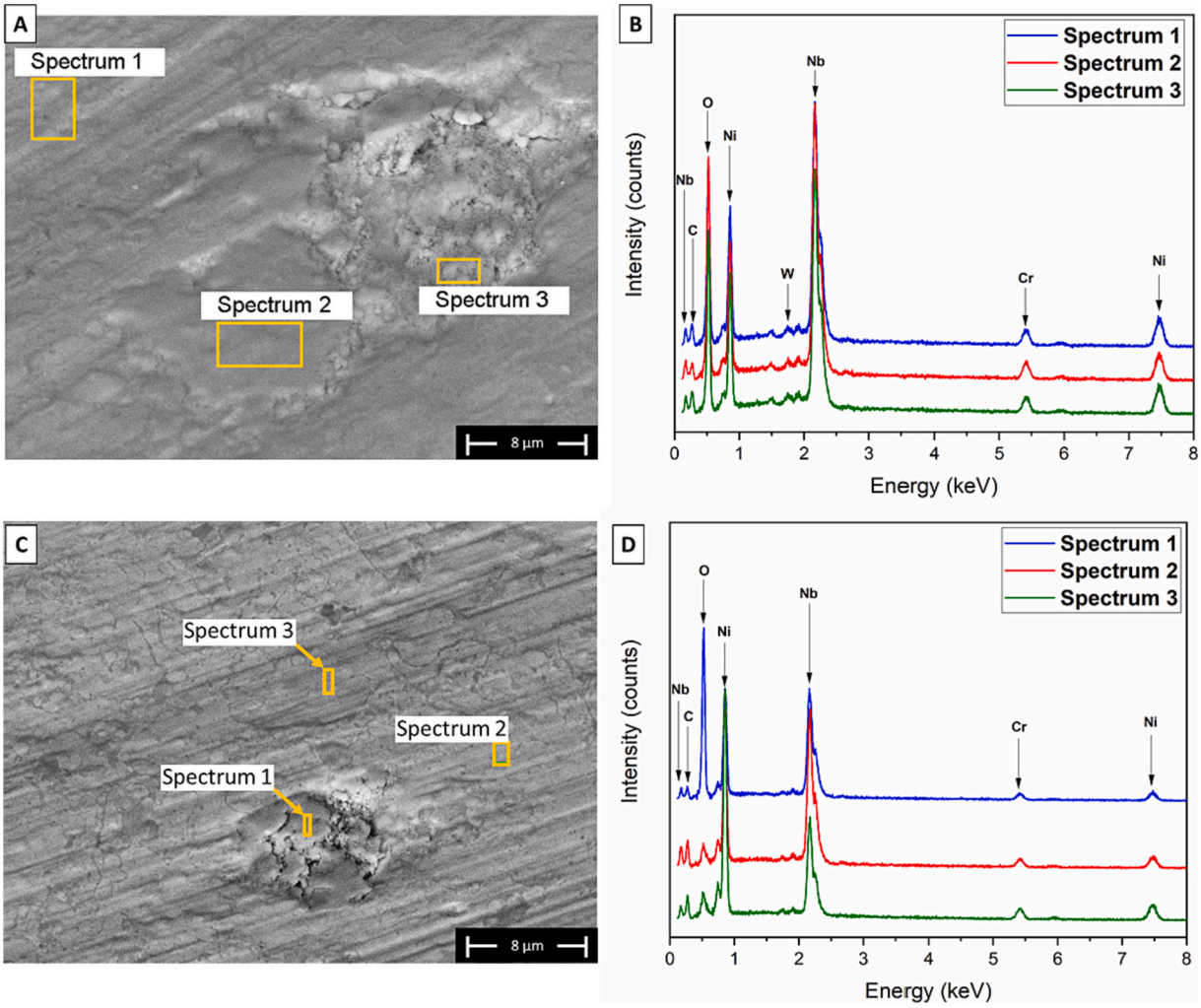

Fig. 18. SEM micrographs of inner zones of the ball-on-disk wear tracks on the NbC-25NiCr set R2 (A) and NbC-40NiCr set R1 (C) coatings after tests at 200 °C, and their corresponding EDX spectra (B, D).

ball does not develop a flattened wear scar: the ball surface mostly retained its original curvature, on top of which the transfer layer was built up. Thus, the wear loss of the ball was not measurable, but in any case, it was clearly much lower than the wear loss of the coating.

According to the SEM images of the NbC-25NiCr-R1, NbC-25NiCr-R2, and NbC-40NiCr-R1 coatings, after sliding wear testing at 200 °C the grooves caused by the asperities of the counterpart or the debris were deeper than at room temperature. Moreover, consistent with the previous observation based on the ball morphology, adhesive wear is evident on the coatings, with ductile tearing visible in Fig. 16 C, E, H and I.

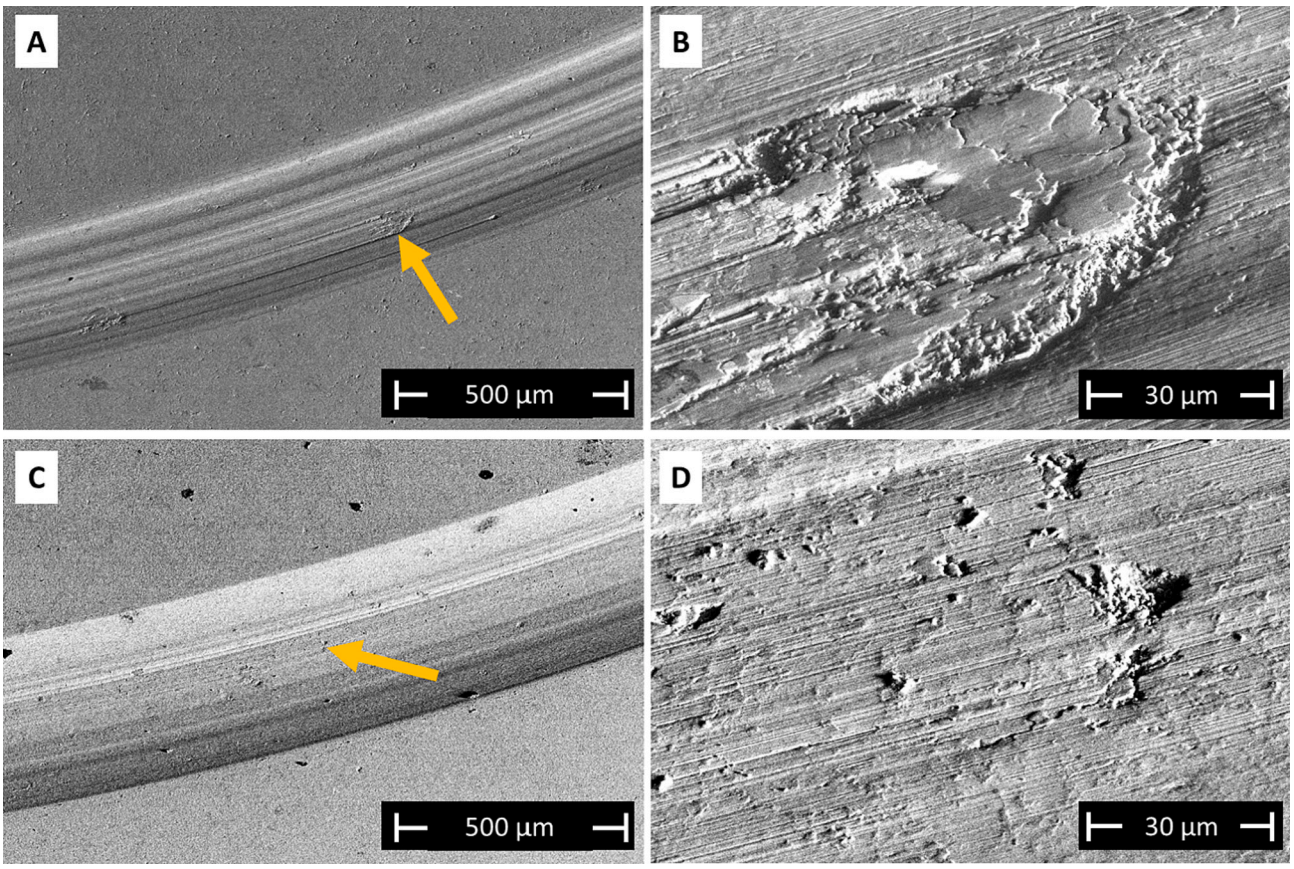

Fig. 19. SEM micrographs of ball-on-disk wear tracks on the NbC-25NiCr set R1 (A, B) and NbC-40NiCr set R1 (C, D) coatings after tests at 400 °C: overviews, with arrows indicating adhesive wear (A, C), and details (B, D).

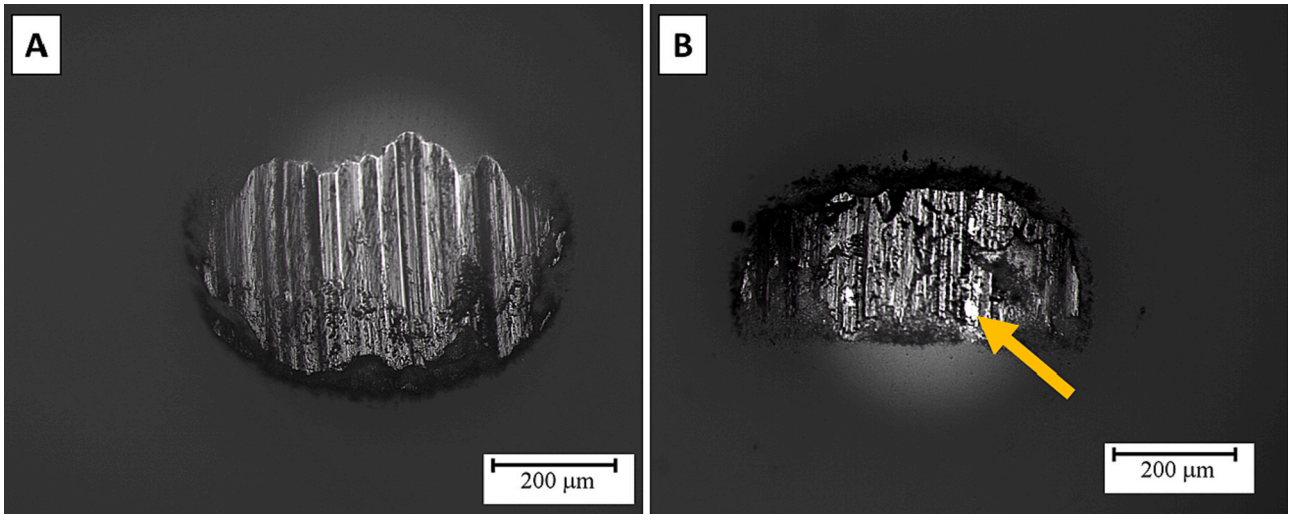

Fig. 20. Optical micrographs of the wear tracks on the Al_2O_3 counterparts after ball-on-disc sliding wear tests at 400 °C against the NbC-25NiCr set R1 (A) and NbC-40NiCr set R1 (B) coatings. The arrow indicates a possible adhesive transfer of the coating to the counterpart.

Brittle delamination is also seen, e.g., in Fig. 16 A, B, with microcracks visible in the detail of Fig. 16 C. Thus, some delamination wear by surface fatigue occurs along with direct adhesive tearing. Surface fatigue is also recognisable from Fig. 17 A, B, which presents deeper microcracks at 200 °C through the cross-sections of wear tracks.

On the other hand, the wear scars seem less covered by patches of tribo-oxidized debris compared to the tests at room temperature, which can further explain the occurrence of adhesive and delamination wear. Accordingly, little (Fig. 18 A, B) or almost no W (Fig. 18 C, D) is found on the coating surface, which is also consistent with the lower (non-measurable) wear loss of the WC-6%Co counterpart, as noted previously.

Where such debris patches were visible, their composition detected by micro-Raman spectroscopy (Fig. 14) was analogous to that seen at room temperature. Namely, the debris consisted of poorly crystalline columbite-type Nb oxides due to tribo-oxidation of the hardmetal debris

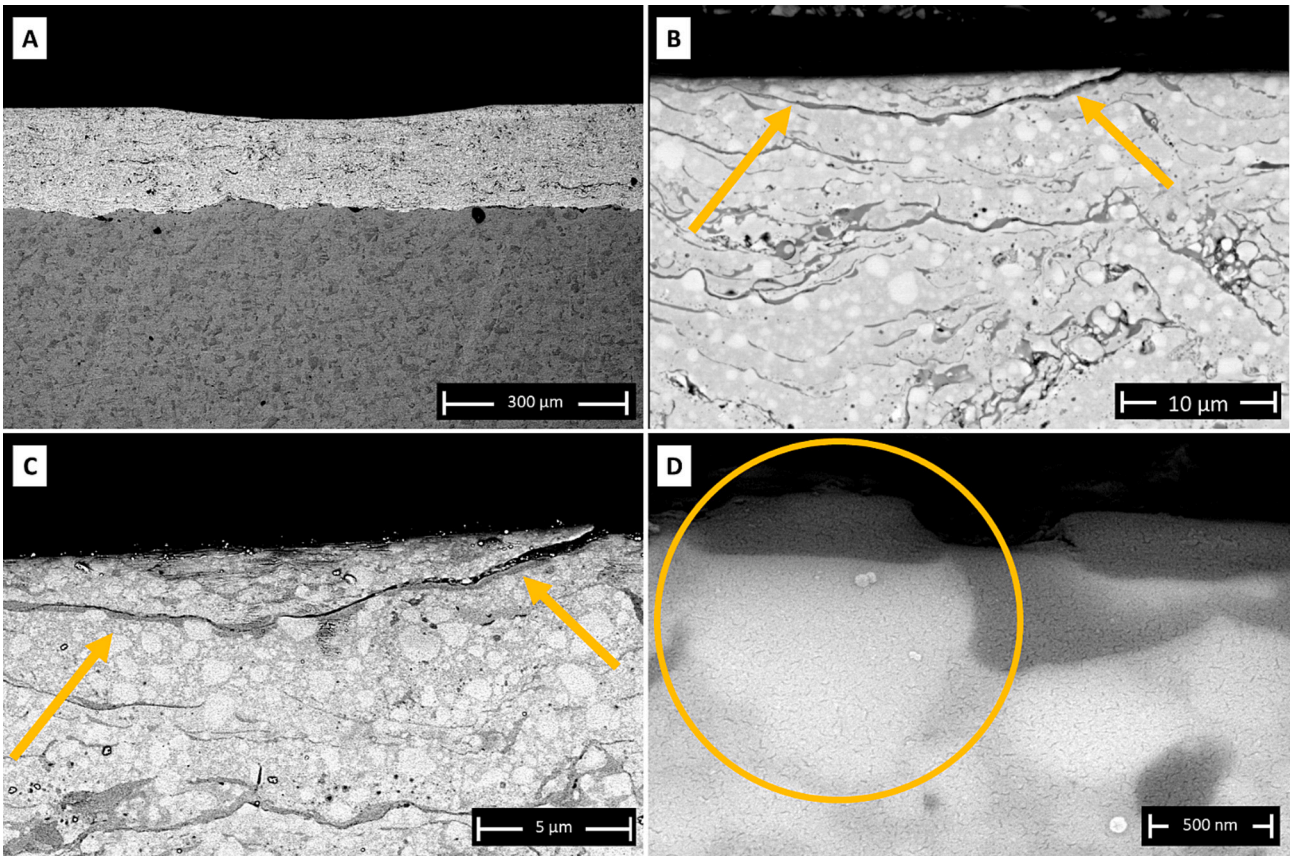

Fig. 21. SEM micrographs of the cross-section of the wear track on NbC-40NiCr set R1 after the test at 400 °C. Low magnification overview (A), magnified views (B, C), and high-magnification detail of the area outside the wear track. Arrows indicate microcracks, and the circle indicates the presence of oxide protrusions on NbC particles.

released by adhesive, abrasive and surface fatigue wear of the coating itself. Note that no oxide scale could be detected outside the wear track at this temperature, since, as shown by the TG-DTA analysis, this temperature is still not sufficient to trigger measurable oxidation of the NbC-NiCr compositions.

3.4.3. *Dry sliding wear resistance at 400 °C*

As noted in Sections 3.4.1 and 3.4.2, in most cases there was little difference between the performance of coatings deposited under distinct conditions. Therefore, further wear tests at 400 °C and 600 °C were performed on the "R1" and "R2" series of NbC-25NiCr and NbC-40NiCr samples, as well as on the TiC-NiCr and Cr_3C_2-NiCr references. WC-CoCr was not employed as it is unsuitable for high-temperature service. For the same reason, Al_2O_3 was used as the counterbody material instead of WC-6%Co. The former represents the hard, inert materials likely to be used as counterfaces in real applications, whilst WC-based hardmetal coatings would not be employed in such conditions.

At 400 °C, the NbC-40NiCr samples exhibit slightly higher specific wear rates [$\approx$ 6–7 $\times$ 10^{-6} $mm^3/(N{\cdot}m)$] compared with the NbC-25NiCr samples [$\approx$ 4–5 $\times$ 10^{-6} $mm^3/(N{\cdot}m)$]. The values are comparable to those of the TiC-25NiCr coatings [$\approx$ 5 $\times$ 10^{-6} $mm^3/(N{\cdot}m)$], but slightly better than the TiC-40NiCr [$\approx$ 1 $\times$ 10^{-5} $mm^3/(N{\cdot}m)$] and Cr_3C_2-NiCr [$\approx$ 3 $\times$ 10^{-5} $mm^3/(N{\cdot}m)$] references (Fig. 8 C). Although the counterpart material was changed, these results suggest the stability of the wear resistance of the NbC-based coatings in the range from 200 °C to 400 °C, while TiC-based coatings show a significant increase in their wear rates in the same range. This is consistent with literature reports on the relatively greater stability of the mechanical properties of NbC with increasing temperature, compared to other types of carbide phases [25].

The average coefficients of friction produced by all coatings against the Al_2O_3 ball at 400 °C (Fig. 9 C) are lower compared to those observed at 200 °C against the WC-Co ball. In detail, the NbC-based coatings produced the largest average friction coefficients ($\approx$0.5–0.6), which are again similar to those reported in the literature for bulk NbC-based hardmetals in unidirectional dry sliding against Al_2O_3 [53]. Lower values were found for the TiC-25NiCr and Cr_3C_2-NiCr references ($\approx$0.4).

The wear track of the NbC-25NiCr-R1 sample (Fig. 19 A-B) is slightly smaller than that of the NbC-40NiCr-R1 sample (Fig. 19 C—D), consistent with the wear rates shown in Fig. 8 C.

Both coatings display deep abrasive grooves and some ductile tearing, indicative of an adhesive wear mechanism. Thus, although the reduced chemical affinity between the hardmetal coating and the counterpart might be one of the reasons why lower friction was observed at 400 °C against Al_2O_3 than at 200 °C against WC-Co, it appears that changing the counterbody did not prevent significant adhesion effects. This is also consistent with the still rather high friction coefficient values of $\approx$0.5–0.6, as noted above.

The cross-section of the wear track on NbC-40NiCr-R1 (Fig. 21 A-D) confirms that some microcracks, indicative of surface fatigue or adhesive tearing, are still present (Fig. 21 B, C). Accordingly, the counterpart is entirely covered by a layer of transferred material, the metallic shine of which further suggests it is not entirely oxidized, consistent with an adhesive wear mechanism. Once again, the wear rate of the counterparts is not measurable and likely negligible as they do not show any surface flattening, i.e., the ball surface retains its curvature, covered by a transfer of material just as it was observed at 200 °C (Fig. 20 A-B).

Considering that oxidation reactions occur in the coating at 400 °C, as confirmed by the thermogravimetric analyses discussed in Section 3.1 (Fig. 4 A-B), EDX analyses were carried out inside (Fig. 22 A-B, E-F) and outside (Fig. 22 C—D, G-H) the wear trace on the NbC-25NiCr-R1 and

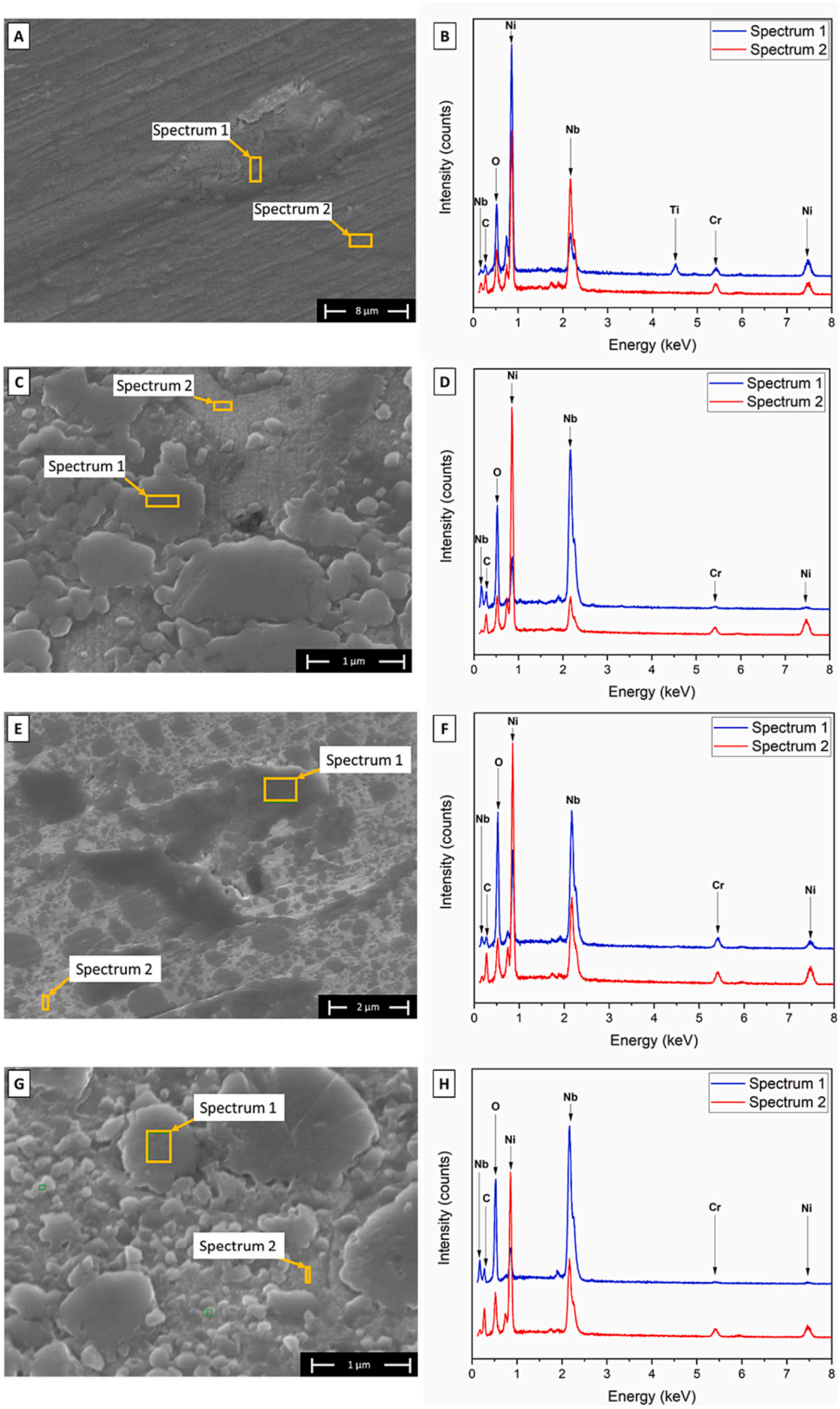

Fig. 22. SEM micrographs of inner (A, E) and outer (C, G) zones in the ball-on-disk wear track on the NbC-25NiCr set R1 (A-D) and NbC-40NiCr set R1 (E-H) coatings after tests 400 °C, and their corresponding EDX spectra (B, D, F, H).

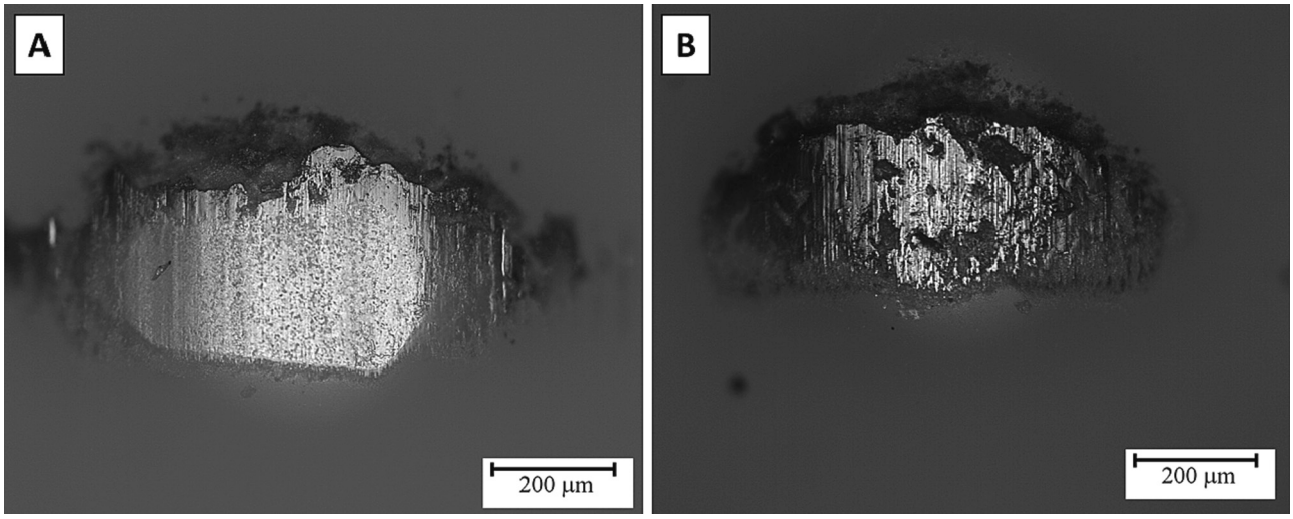

Fig. 23. Optical micrographs of the wear tracks on the Al_2O_3 counterparts after ball-on-disc sliding wear tests at 600 °C against the NbC-25NiCr set R1 (A) and NbC-40NiCr set R1 (B) coatings.

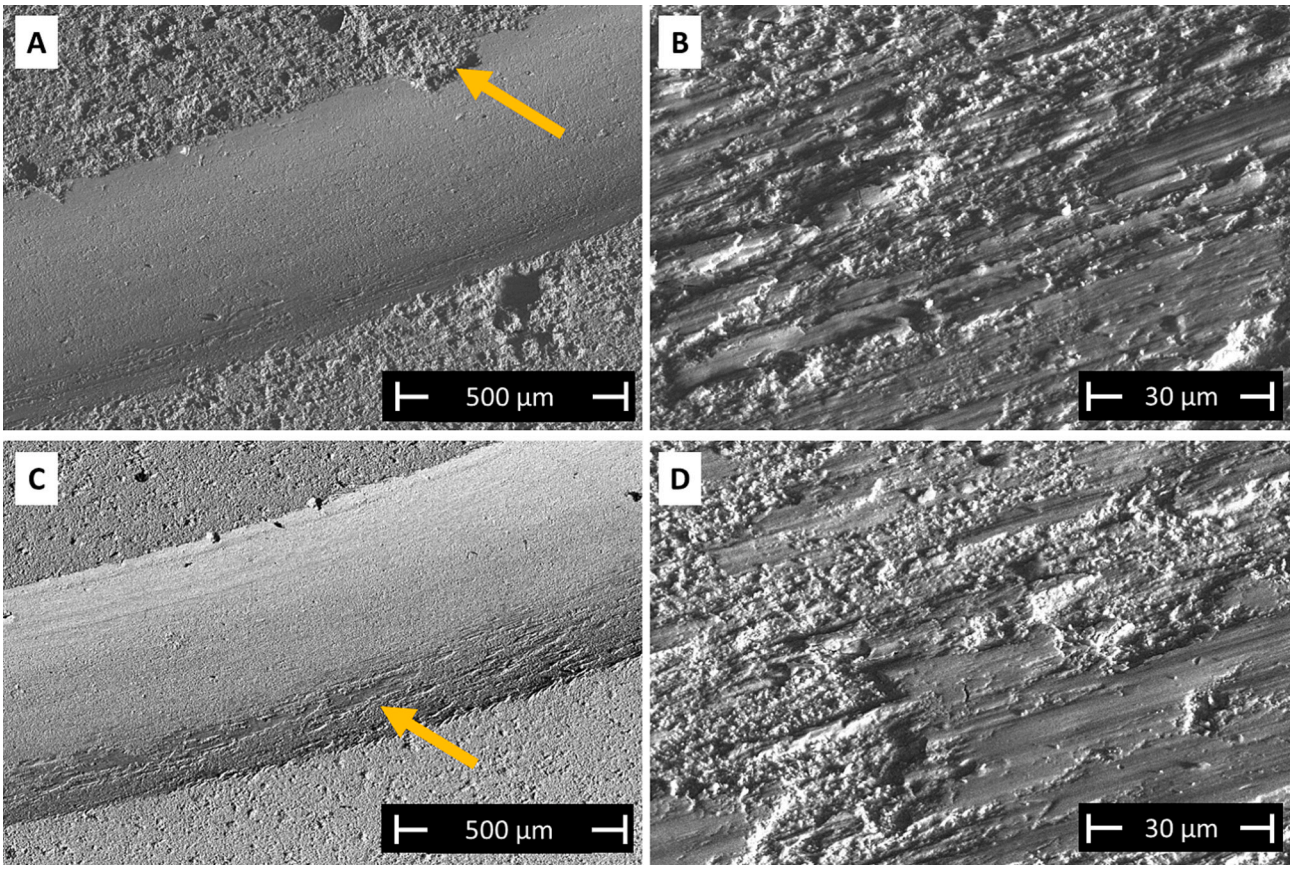

Fig. 24. SEM micrographs of ball-on-disk wear tracks of the NbC-25NiCr set R1 (A, B) and NbC-40NiCr set R1 (C, D) coatings after 600 °C tests: overviews, with arrows indicating the predominance of a layer of oxides superimposed on the wear track (A, C), and details (B, D).

NbC-40NiCr-R1 coatings after sliding wear testing at 400 °C.

Outside the wear track, exposure to high temperature throughout the test duration caused preferential oxidation of the NbC particles, which develop distinctively recognisable protrusions. The EDX spectra accordingly confirm that the protrusions (Fig. 22 C, D – Spectrum 1, Fig. 22 G, H – Spectrum 1) consist of Nb and O, with little signal from the matrix elements (Ni, Cr). By contrast, spectra acquired on the surrounding matrix (Fig. 22 C, D – Spectrum 2, Fig. 22 G, H – Spectrum 2) show a more significant proportion of Ni and Cr and a much lower amount of oxygen, indicating that the oxide scale on the matrix (if any) is thin. Micro-Raman spectra acquired on this outer scale (Fig. 14) accordingly reveal broad bands due to Nb-O-Nb bonds, as well as a possible contribution by (Ni, Cr)-based spinels that might have been developed on the matrix [55]. It should be remarked that the sub-micrometric size of individual NbC particles is smaller than the lateral resolution of the micro-Raman technique (~1 µm), so that both the

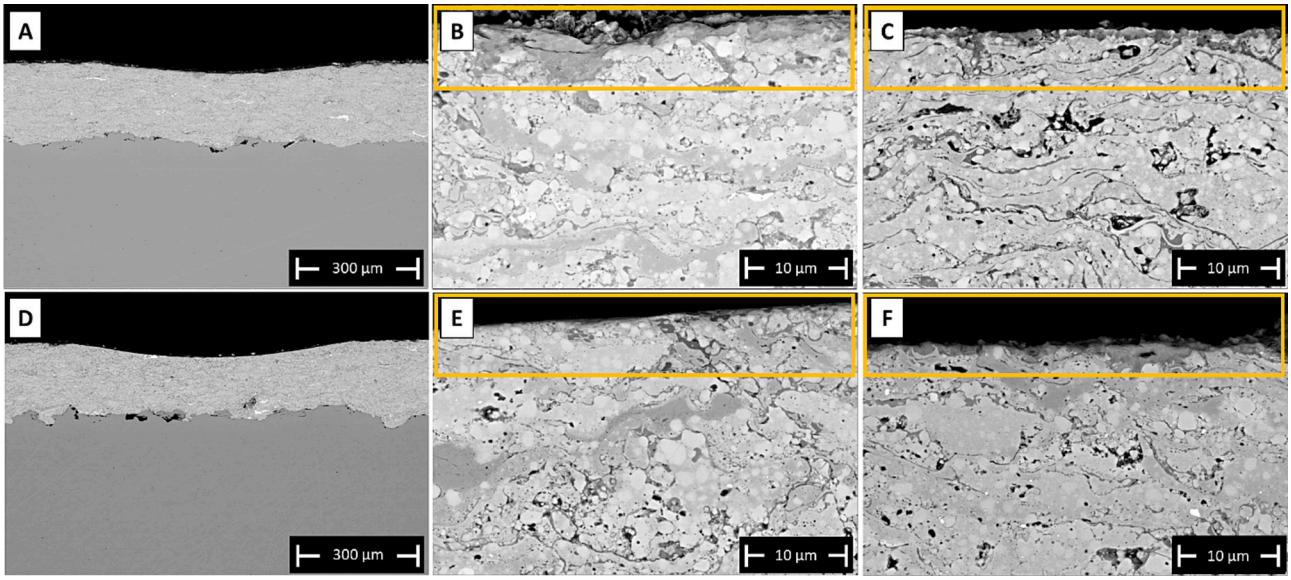

Fig. 25. SEM micrographs of the cross-section of the wear track on the NbC-25NiCr set R1 (A-C) and NbC-40NiCr set R1 (D—F) coatings after tests at 600 °C. Low magnification overview (A, D), intermediate magnification inside the wear track (B, E) and intermediate magnification outside the wear track (C, F). Rectangles indicate the presence of an oxide film.

oxide scale on the NbC particles and that on the matrix enter the Raman spectra acquired on this surface.

Cross-sections of the oxidized samples also confirm that oxide protrusions (with a thickness well below 1 µm) are visible only on the NbC particles (Fig. 21 D), whilst any scale on the matrix is too thin to be detectable.

During sliding, the thin oxide layer formed on the NbC particles is removed; accordingly, protrusions selectively located on those particles are no more visible (Fig. 22 E, F). On the other hand, tribo-oxidized patches are sometimes visible on the worn surface (Fig. 22 E, F – Spectrum 1) or inside the worn pits (Fig. 22 A, B – Spectrum 1). As these oxides were formed by tribo-oxidation of wear debris coming from both the carbide and matrix phases, they contain Nb, Ni and Cr in similar proportions as in the overall composition of the coating, thus differing from the pristine Nb-based oxides found outside the track. Their Raman spectrum is consistently different from that of the outer scale and analogous to that seen in the debris patches found at room temperature and 200 °C (Fig. 14).

3.4.4. *Dry sliding wear resistance at 600 °C*

Going from 400 °C to 600 °C, the specific wear rates of the TiC-40NiCr and Cr_3C_2-NiCr coatings do not increase much, remaining in the range of 1–2 × 10^{-5} $mm^3/(N{\cdot}m)$, whereas the specific wear rates of all other coatings, including the NbC-NiCr ones, increased by about one order of magnitude. As a result, at 600 °C, all coatings show similar wear rates (Fig. 8 D).

Likewise, at 600 °C, there is no significant difference between the average friction coefficients (≈ 0.5) produced by the coatings based on NbC and TiC, which are slightly higher than the value detected with the Cr_3C_2-NiCr coating (≈ 0.4) (Fig. 9 D).

The SEM images of the NbC-25NiCr-R1 (Fig. 24 A-B) and NbC-40NiCr-R1 (Fig. 24 C—D) coatings subjected to wear at 600 °C indicate the predominance of an oxide layer superimposed on the coatings of both compositions, which would suggest a predominant tribo-oxidation wear mechanism. By contrast, abrasive grooves are not as noticeable as at lower temperatures. An intense oxygen peak was detected in all EDX spectra (Fig. 26), thus confirming the widespread presence of an oxide film on the worn surfaces. Cross-sectional views also confirm the presence of an oxide film on top of the wear scar (Fig. 25).

However, the optical micrographs of the alumina (Al_2O_3) counterparts (Fig. 23 A-B), which do not exhibit any significant wear, reveal the substantial transfer of at least partly non-oxidized material. This indicates that adhesive wear is still occurring at 600 °C, in contrast with the surface appearance of the samples.

This discrepancy can be explained by considering that, during furnace-cooling of the sample at the end of the wear test, spontaneous oxidation of the wear track likely occurred, thus altering its appearance and covering any extant signs of adhesive as well as abrasive wear. The oxidation rate of the coatings at 600 °C was indeed significantly higher than at 400 °C, as revealed by TG-DTA analyses.

Still, as this temperature was barely at the onset of the second oxidation peak seen in the DTA and DTG curves of Fig. 4, the composition of the oxide scale formed spontaneously outside the wear track is once again based on Nb oxides. Notably, the Raman spectrum acquired inside the wear track after the test at 600 °C is a bit different from the spectra of the tribo-oxidized debris clusters formed at all other temperatures. It is more similar to the Raman spectrum of the outer scale formed at 400 °C. This would corroborate the assumption that the worn surface oxidized while cooling slowly to room temperature, so that at least part of the scale seen in Fig. 24 A, C (surface) and Fig. 25 B, E (section) is just a product of such post-oxidation.

Thus, unfortunately it is more difficult to draw clear conclusions on the exact nature of the wear mechanisms occurring at 600 °C. In any case, partial mediation of the contact by a tribofilm was possible, despite the occurrence of some adhesive wear as previously inferred from the Al_2O_3 surface. This can explain why the friction coefficient measured at 600 °C is, in some cases, even lower than at 400 °C.

Despite the limited literature available on NbC-based coatings and the absence of prior studies on HVOF-sprayed NbC-NiCr, some previous work addressed the tribological performance of bulk hardmetals consisting of niobium carbide. Woydt et al. [30,56,57] evaluated the tribological behaviour of discs made of NbC-8Co, NbC-12Co, and NbC-FeAl by the spark plasma sintering (SPS) process. They carried out unidirectional dry sliding wear tests with sintered alumina counterparts (99.7 %) over a speed range from 0.1 m/s to 8.0 m/s, at temperatures of 22 °C and 400 °C, with a load of 10 N and a sliding distance of 5000 m. Under the same speed conditions (0.4 m/s) as in the test that we carried out with the NbC-NiCr coatings in this paper, the sintered hardmetal discs produced higher values of friction coefficients at low temperatures (≈ 0.9–1) and friction coefficients in the range of ≈0.6–1 at 400 °C,

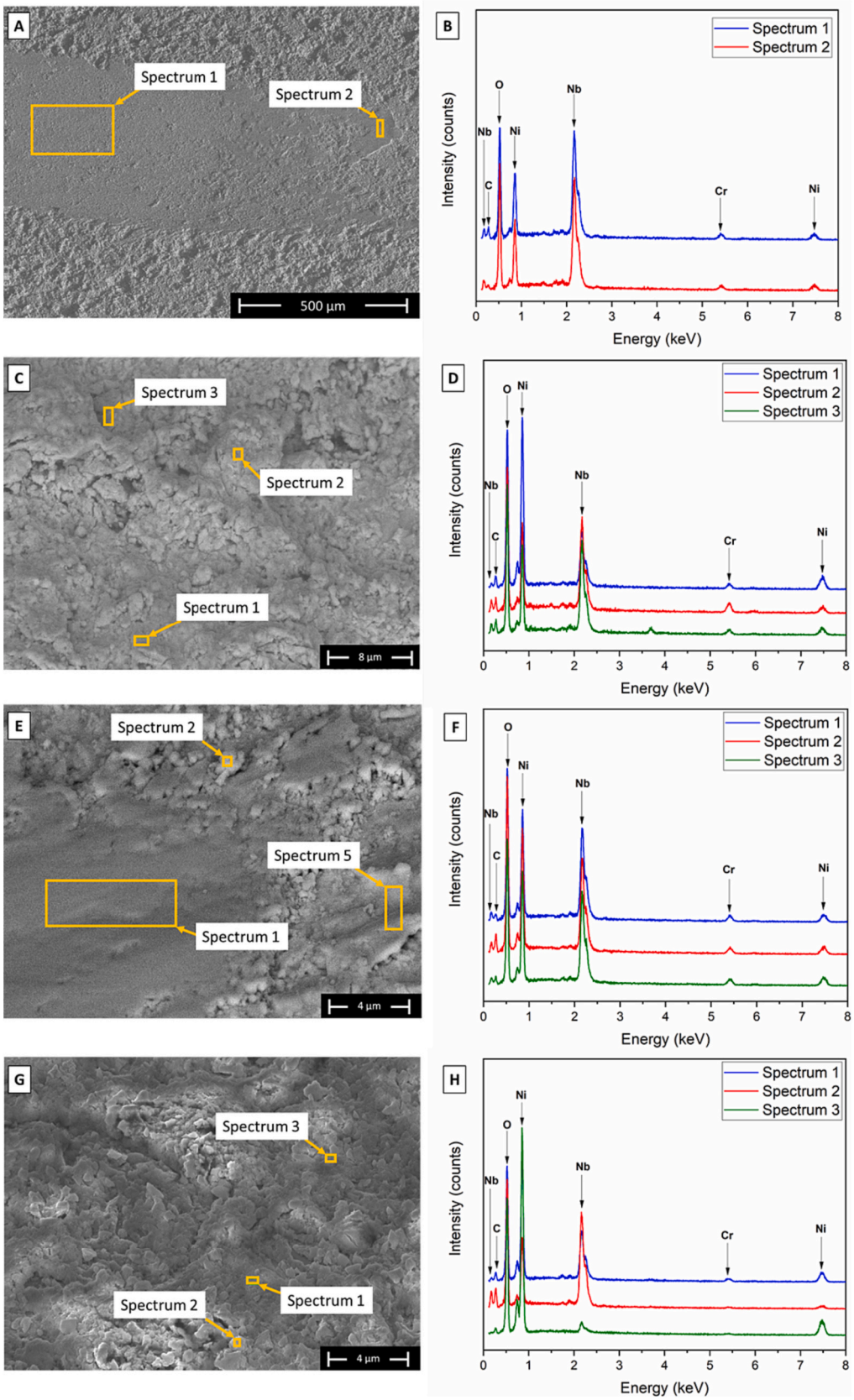

Fig. 26. SEM micrographs of inner (A, E) and outer (C, G) zones of the ball-on-disk wear tracks on the NbC-25NiCr set R1 (A-D) and NbC-40NiCr set R1 (E-H) coatings after tests at 600 °C, and their corresponding EDX spectra (B, D, F, H).

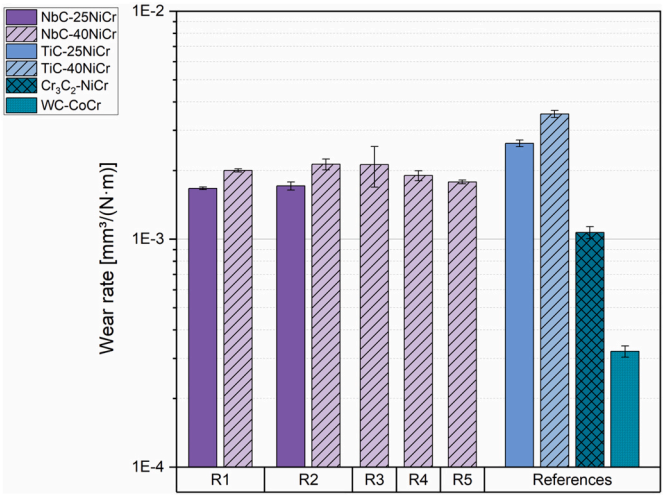

Fig. 27. Wear rates measured after dry sand-steel wheel abrasion testing of all samples, using Al_2O_3 (185 μm) abrasive, 100 g/min flow rate and 40.2 N load.

while the wear rates were of the order of $\approx 10^{-6}$ mm^3/(N·m) at 22 °C and $\approx 10^{-6}$–10^{-5} mm^3/(N·m) at 400 °C. Despite the difference with our ball-on-disc test conditions, these results show similar friction coefficients at low temperatures and a common tendency for these coefficients to decrease with increasing temperature. In contrast, the sintered discs showed slightly higher specific wear rates than our HVOF-sprayed NbC-NiCr coatings.

3.5. Abrasive wear resistance

The abrasive wear rates obtained for the NbC-25NiCr and NbC-40NiCr coatings can be seen in the comparative histogram with the other reference coatings (Fig. 27). The results showed no significant difference between the various NbC-based coatings. All samples showed an abrasive wear rate of $\approx 2 \times 10^{-3}$ mm^3/(N·m). These values are slightly lower than those observed in TiC-based coatings [$\approx 3 \times 10^{-3}$ mm^3/(N·m)] and slightly higher than those measured for the Cr_3C_2-NiCr coating [$\approx 1 \times 10^{-3}$ mm^3/(N·m)]. A notable difference can be seen in the case of the WC-CoCr reference coating, which has a significantly lower abrasive wear rate than all other samples [$\approx 3 \times 10^{-4}$ mm^3/(N·m)].

The better resistance to abrasive wear of the NbC-NiCr coatings compared with the TiC-NiCr coatings can be caused by their higher microhardness and elastic modulus, also because these properties are correlated with the intra-lamellar and inter-lamellar cohesion [58]. In this same perspective, WC-CoCr presumably shows better resistance to abrasive wear due to its high hardness, stronger interlamellar cohesion, as well as stronger bonding between WC and the CoCr matrix [59].

In Figs. 28 and 29, SEM micrographs of the surfaces of the NbC-25NiCr-R1 (Fig. 28 A-C, Fig. 29 A) and NbC-40NiCr–R1 (Fig. 28 D—F, Fig. 29 C) coatings after abrasive wear are shown at different magnifications. Both ductile and brittle forms of abrasion are recognisable. Abrasive grooves are due to ductile abrasion mechanisms (ploughing and/or cutting) and occur where lamellar cohesion is more substantial and/or in matrix-rich lamellae, such as shown in Fig. 5. The SEM micrographs and the EDX spectra reported in Fig. 29 A, B (spectrum 3) and Fig. 29 C, D (spectrum 1) also show alumina particles incorporated into the worn surface, which is due to a ductile indentation mechanism typical of a three-body abrasion phenomenon. On the other hand, brittle delamination can also be recognized, especially in the magnified views (panels C, F in Fig. 28 and Fig. 29 A – Spectrum 1). The brittle fracture might affect Nb-rich splats (see the different relative intensities between Nb peaks and Ni, Cr peaks in spectrum 1 and spectrum 2 of Fig. 29 A, B) and/or it can be promoted by the presence of oxide stringers along lamellar boundaries, which would undoubtedly facilitate interlamellar crack propagation. The occurrence of a brittle form of abrasive wear, especially when compared to HVOF-sprayed WC-CoCr coatings that do not exhibit such phenomenon under the same test conditions [34], can explain the substantially higher specific wear rates under three-body abrasion conditions.

3.6. Corrosion resistance

The results obtained from the analysis of electrochemical polarization curves (Fig. 30) are reported in Table 5. The NbC-40NiCr coatings have better corrosion resistance compared to the NbC-25NiCr ones, according to their respective ranges of corrosion current density ($\approx$ 0.55–1.46 μA/cm^2 and $\approx$ 0.07–0.39 μA/cm^2) and corrosion potential ($\approx$ −354 to −270 and $\approx$ −285 to −76 mV vs. Ag/AgCl/KCl$_{(sat.)}$).

In general, comparing the results of the NbC-25NiCr and NbC-40NiCr

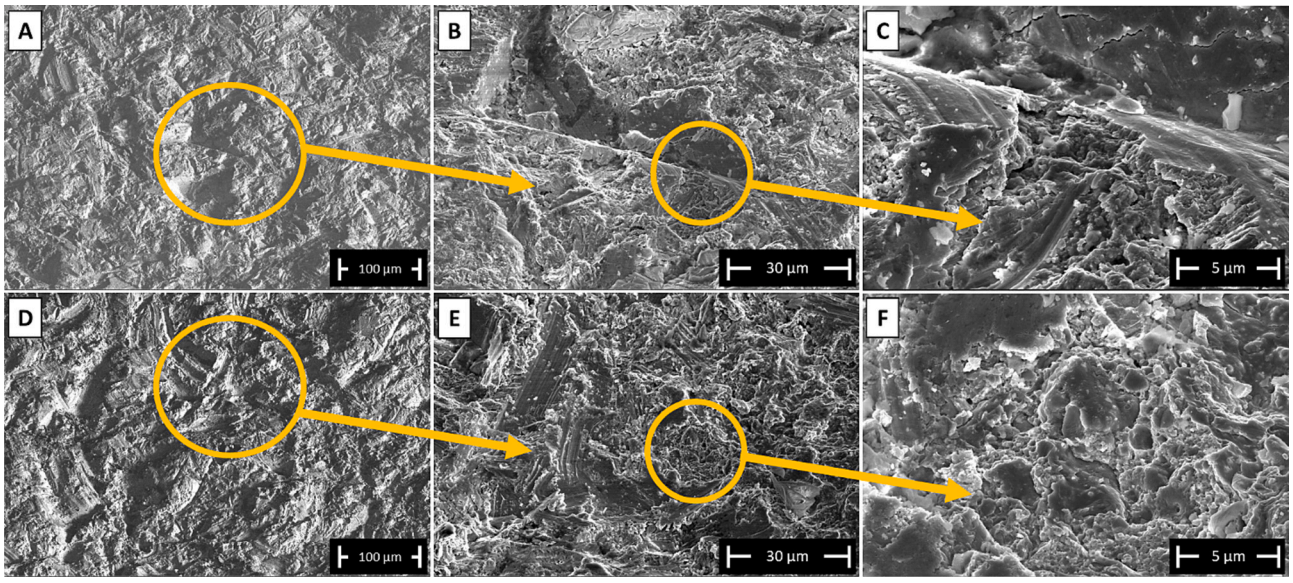

Fig. 28. SEM micrographs of the NbC-25NiCr set R1 (A-C) and NbC-40NiCr set R1 (D—F) coatings after dry sand-steel wheel abrasion testing: low magnification overviews (A, D), intermediate (B, E) and high-magnification (C, F) details.

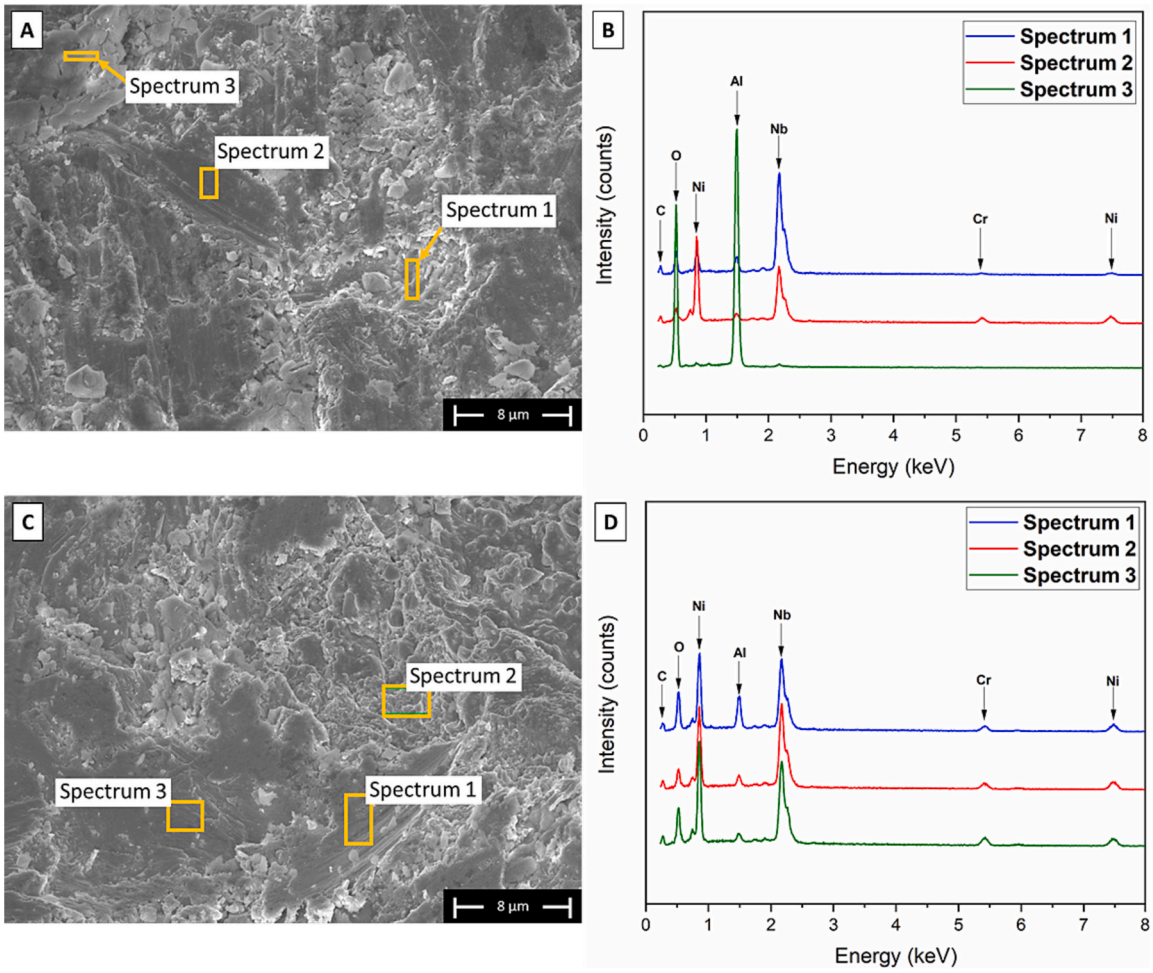

Fig. 29. SEM micrographs of the NbC-25NiCr set R1 (A) and NbC-40NiCr set R1 (C) coatings after dry sand-steel wheel abrasion testing and their corresponding EDS spectra (B, D).

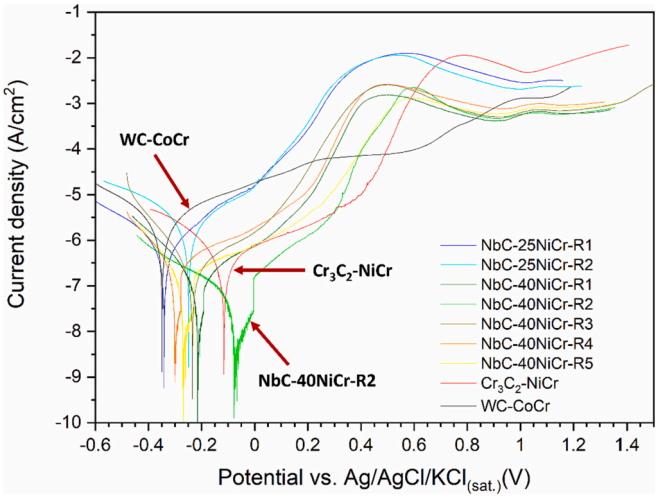

Fig. 30. Electrochemical polarization curves of all samples with NbC-based coatings and the Cr_3C_2-NiCr and WC-CoCr references.

coatings with the reference coatings (Table 5), it is seen that both NbC-based coatings are significantly more resistant to corrosion and more noble than WC-CoCr, which has higher corrosion current density value and lower corrosion potential. Compared to TiC-based coatings, NbC-based coatings (considering the corresponding matrix concentrations) are also more resistant. The outstanding performance of the NbC-40NiCr composition is notable, as it presents better corrosion resistance than the conventional Cr_3C_2-NiCr coating. Its performance approaches that of uncoated, polished AISI 304 stainless steel, whose corrosion current density, tested by the authors under identical conditions in a previous work, is 0.07 ± 0.01 µA/cm^2.

As previously observed in the electrochemical polarization curves of TiC-NiCr coatings [22], the NbC-40NiCr coatings also present a passivity regime with a current density ≤ 1 µA/cm^2 with subsequent transpassivation. The considerable similarity between the electrochemical polarization curves of these materials indicates that passivity and transpassivation phenomena affect the matrix.

Indeed, the SEM micrographs in Fig. 31 showed that, at the end of the electrochemical polarization test (i.e. directly after the application of the highest anodic overpotential), corrosion damage affected the matrix. The magnified views in Fig. 31 B, C, E, F, H, I, K, L show the unaltered, fine NbC particles left almost unsupported amidst a corroded matrix. Through the EDX analyses (Fig. 32 A, B – Spectrum 1, 2 and 3, Fig. 32 C, D – Spectrum 1 and 3, Fig. 32 E, F – Spectrum 1, 2 and 3), it is possible to confirm that the process of selective corrosion of the matrix occurs with the selective leaching of nickel. The spectra reveal a decrease or disappearance of the Ni peaks in the corroded regions of the coatings (Fig. 32 B, D, F, H).

The anodic polarization curves of the NbC-25NiCr samples, despite their qualitatively similar behaviour, do not exhibit proper passivation, with slowly increasing current density values in the range of 1–10 µA/

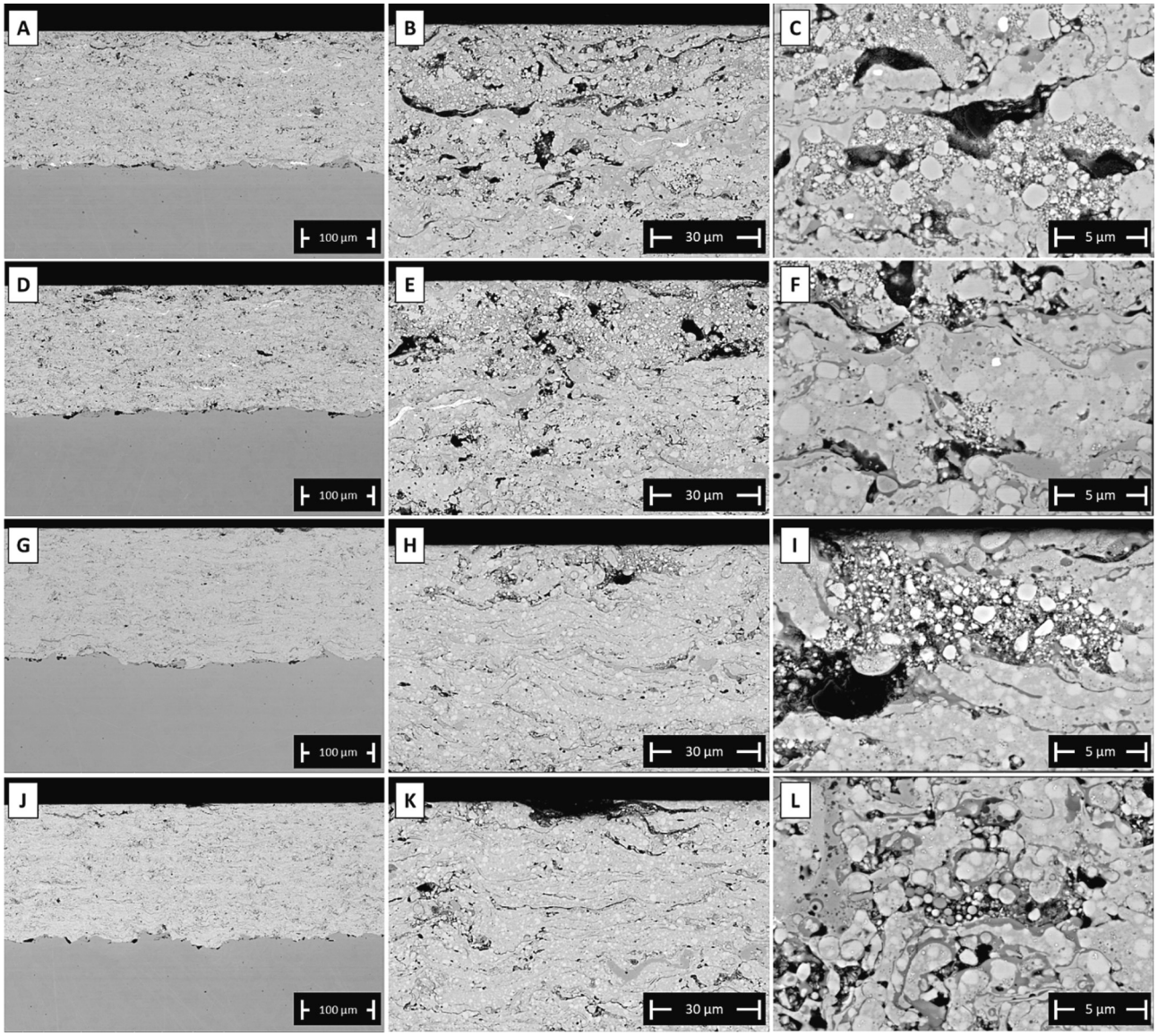

Fig. 31. SEM micrographs of the cross-section of NbC-25NiCr-R1 (A-C), NbC-25NiCr-R1 (D—F), NbC-40NiCr-R1 (G-I) and NbC-40NiCr-R2 (J-L) samples after electrochemical polarization tests: low magnification overviews (A, D, G, J), intermediate (B, E, H, K) and high-magnification (C, F, I, L) details.

cm^2 up to a potential of around 0 V vs. $Ag/AgCl/KCl_{(sat.)}$. Therefore, fewer areas were affected by corrosion in the cross-sectional micrographs of the NbC-40NiCr coatings (Fig. 31 G-L) compared to NbC-25NiCr coatings set R1 and R2 (Fig. 31 A-F).

Through the SEM micrographs, it is also possible to observe that the corrosion process does not occur at the interface with the substrate, being located only in the regions of the coating close to the surface, which confirms the protectiveness and denseness of these samples.

Micrographs of TiC-NiCr coatings after the electrochemical polarization test under the same conditions as the NbC-NiCr coatings [22] showed comparatively more severe matrix dissolution at the end of the same anodic polarization test. It is possible to speculate that the dissolution of some Nb in the NiCr matrix (see the previous comments in Section 3.2 related to the shift of the XRD peaks of the matrix after HVOF spraying) benefited its passivation ability more than did the dissolution of Ti in the TiC-NiCr compositions. This can explain why the corrosion current density, the passive current density, and even the current density in the transpassive regime of the NbC-40NiCr coatings are one order of magnitude lower than the corresponding values for TiC-40NiCr coatings (Fig. 30).

Another interesting observation in the comparison between coatings based on TiC and NbC is the lower resistance to corrosion of the compositions richer in carbides (TiC-25NiCr and NbC-25NiCr) compared to the compositions with 40 vol% of NiCr, indicating that in both cases micro-galvanic couples are established between the nobler carbide phase (NbC or TiC) and the less noble metallic phase (NiCr). According to Luiz et al. [60], the damage caused by galvanic corrosion can be increased when the area of the cathode grows with respect to the anode. Thus, the compositions with higher carbide content are more affected.

Comparing the overall performance of the studied coatings, it is also possible to observe a better resistance to corrosion of the coatings with a NiCr binder phase compared to the CoCr matrix of the WC-CoCr sample. This behaviour can be explained by the lower corrosion resistance of cobalt compared to nickel [61]. According to Sutthiruangwong et al. [62], no passive film is detectable in the “pseudo-passive” regime of WC-CoCr, which accordingly occurs with higher corrosion current density than the other coatings that form passive films, as seen in Fig. 30. The pseudopassivity of WC-CoCr can be explained by the decrease in the corrosion current density due to the permanence of a porous WC skeleton after matrix oxidation, which slows down the diffusion velocity of

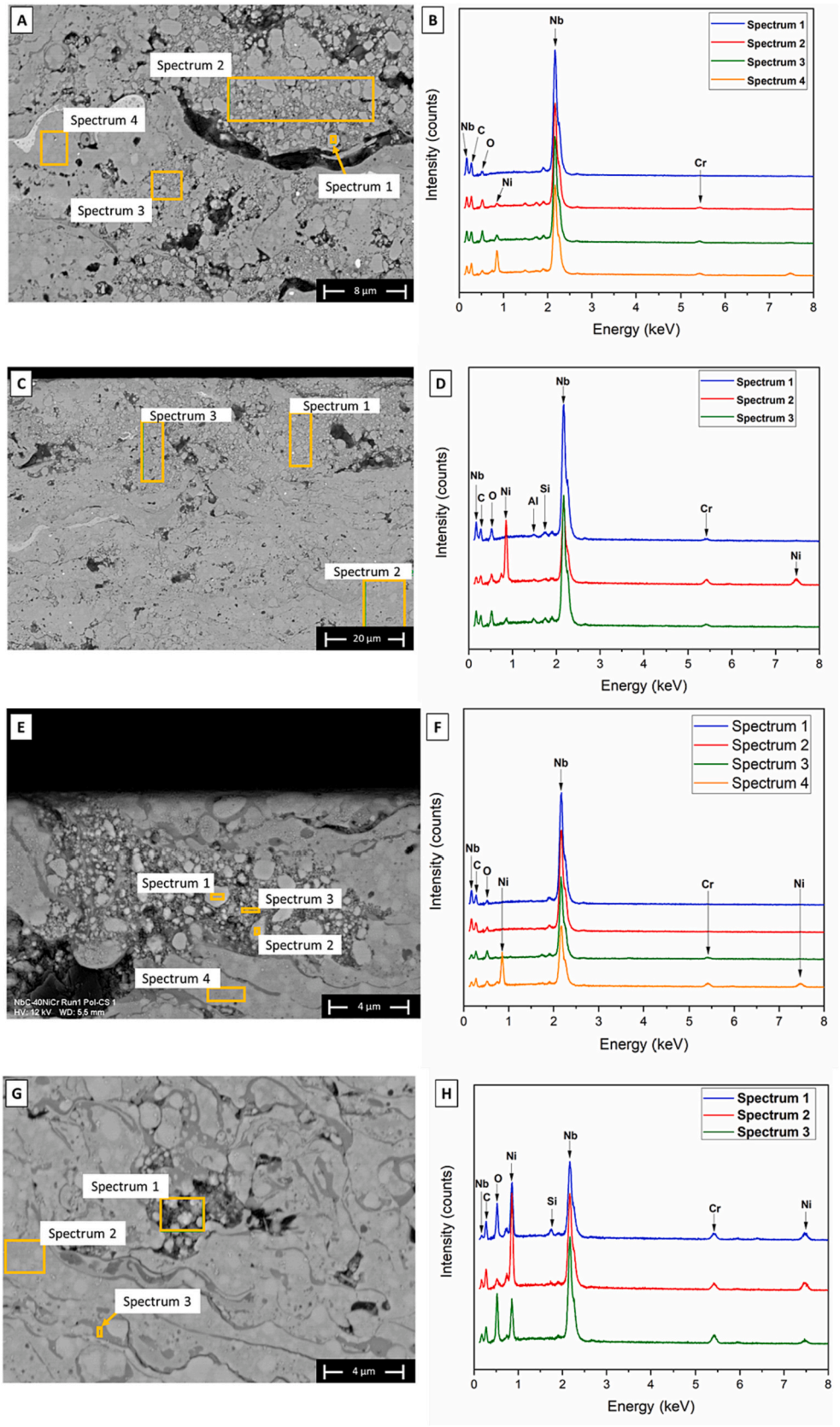

Fig. 32. SEM micrographs of the cross-section of NbC-25NiCr-R1 (A), NbC-25NiCr-R2 (C), NbC-40NiCr (E) and NbC-40NiCr (G) samples after electrochemical polarization tests, and their corresponding EDX spectra (B, D, F, H).

Table 5
Corrosion current density and corrosion potential values of NbC-25NiCr and NbC-40NiCr coatings and the Cr_3C_2-NiCr, TiC-NiCr and WC-CoCr references.

Coating	Set	I_{Corr} [μA/cm^2]	E_{Corr} [mV]
NbC-25NiCr	R1	0.55 ± 0.03	−354 ± 20
	R2	1.46 ± 0.56	−270 ± 26
NbC-40NiCr	R1	0.13 ± 0.02	−260 ± 67
	R2	0.07 ± 0.01	−76 ± 5
	R3	0.19 ± 0.07	−240 ± 5
	R4	0.24 ± 0.06	−285 ± 18
	R5	0.14 ± 0.01	−256 ± 11
Cr_3C_2-NiCr	–	0.39 ± 0.02	−130 ± 35
WC-CoCr	–	1.86 ± 0.46	−360 ± 14
TiC-25NiCr [22]	–	0.75 ± 0.01–1.77 ± 0.57	(−337 ± 11) – (−243 ± 32)
TiC-40NiCr [22]		0.16 ± 0.01–0.45 ± 0.11	(−270 ± 2) – (−104 ± 8)
AISI 304 [22]		0.07 ± 0.01	- 64 ± 15

Co^{2+} ions (anodic polarization residues).

4. Conclusions

The performance of new HVOF-sprayed coatings based on niobium carbide, obtained from high-energy ball milled (HEBM) feedstock powders with NbC -25 vol% (Ni – 20 wt% Cr) and NbC - 40 vol% (Ni – 20 wt%Cr) compositions, was assessed in this work.

The microstructure and the properties of the coatings were compared with WC-CoCr and Cr_3C_2-NiCr reference coatings obtained from commercially available feedstock powers, as well as with TiC-NiCr coatings that were also produced using HEBM feedstock powders and have the same volumetric fractions of metallic matrix as the NbC-NiCr coatings.

The most important conclusions are as follows:

- All NbC-NiCr coatings were microstructurally similar, except for the lower porosity of the NbC-40NiCr coating deposited with the R1 parameter set. Anyway, all NbC-based coatings exhibited <1 % porosity, which is slightly lower than that found in the TiC-NiCr coatings.
- The NbC-based coatings also showed slightly higher Vickers microhardness than the TiC-based coatings with corresponding matrix volume fractions. These hardness values were also comparable to or slightly higher than the values listed in the literature for Cr_3C_2-NiCr, but lower than the hardness of the WC-CoCr coating. The NbC-40NiCr composition has greater microhardness (≈1000 $HV_{0.3}$) than the NbC-25NiCr composition (≈ 900 $HV_{0.3}$). This was ascribed to the brittleness of compositions with low matrix content.
- Ball-on-disc tests carried out at room temperature against a WC-6% Co counterpart did not reveal any significant differences among the specific wear rates obtained for both NbC-NiCr compositions. Abrasion and tribo-oxidation were the main wear mechanisms. Values in the range of 2–4 × 10^{-7} mm^3/(N·m) have the same order of magnitude as those of the TiC-NiCr coatings and are intermediate between those produced by WC-CoCr and Cr_3C_2-NiCr reference coatings.
- Higher friction coefficients were produced by the NbC-based coatings (≈ 0.7–0.8) than by all other references.
- At 200 °C, the specific wear rates of the NbC-based coatings increased whilst the coefficients of friction remained high. Deeper abrasive grooves as well as adhesive wear and brittle delamination were detected at this temperature.
- At 400 °C, slightly lower wear rates and slightly higher friction coefficients against an Al_2O_3 counterpart were observed for the NbC-25NiCr composition in comparison with the NbC-40NiCr one. Differences were anyway small, and the specific wear rates were similar to those produced by the TiC-25NiCr coating. Compared to the specific wear rates measured at 200 °C (against WC-6%Co), the values did not increase much. The TiC-40NiCr and Cr_3C_2-NiCr reference coatings wore comparatively more under the same test conditions and TiC-40NiCr also exhibited a greater increase in wear loss from 200 °C. Wear mechanisms were also similar to those at 200 °C, with abrasive grooving, some adhesive wear, and some surface fatigue, in addition to tribo-oxidation.
- At 600 °C, all NbC-based coatings showed similar wear rates. Wear mechanisms, however, could not be assessed because the worn surface oxidized while the sample was cooling down after the test.
- The NbC-NiCr coatings exhibited high specific wear rates of ≈2 × 10^{-3} mm^3/(N·m) in the dry particles' abrasion test. This was caused by brittle abrasion phenomena in addition to ductile grooving. Thus, they are not suitable for high-stress abrasion conditions.
- Finally, both the NbC-25NiCr and the NbC-40NiCr compositions are more resistant to corrosion than the WC-CoCr coating and, considering the same matrix concentrations, they also show greater corrosion resistance than the TiC-NiCr coatings. NbC-40NiCr samples particularly stand out for having better corrosion resistance even when compared to the Cr_3C_2-NiCr reference.

Overall, the results indicate that NbC-based coatings are promising alternatives for applications that require a balance of wear resistance and corrosion, and/or for applications at intermediate and high temperatures.

Research on bulk hardmetals showed that further tailoring the composition of the matrix and the hard phase with proper additions of e.g. Mo, VC, TiC might further improve the mechanical properties (hardness / toughness balance) and wear resistance of NbC-based hardmetals with Ni-based matrices [25,63–65]. While such compositional refinements were outside the scope of the present work, this topic could be tackled in future works.

CRediT authorship contribution statement

Larissa Rossi Gehlen: Conceptualization, Methodology, Investigation, Formal analysis, Data curation, Writing – original draft. **Giovanni Bolelli:** Conceptualization, Methodology, Investigation, Formal analysis, Data curation, Writing – review & editing, Supervision. **Pietro Puddu:** Methodology, Investigation. **Enrico Forlin:** Methodology, Investigation. **Alberto Colella:** Methodology, Investigation. **Giuseppe Pintaude:** Conceptualization, Methodology, Resources, Writing – review & editing, Supervision. **Luca Lusvarghi:** Conceptualization, Methodology, Resources, Writing – review & editing, Supervision.

Declaration of competing interest

The authors declare the following financial interests/personal relationships which may be considered as potential competing interests: Enrico Forlin reports a relationship with MBN Nanomaterialia SpA that includes: employment. Alberto Colella reports a relationship with MBN Nanomaterialia SpA that includes: employment.

Data availability

Data will be made available on request.

Acknowledgements

The authors acknowledge CBMM (Cia. Brasileira de Metalurgia e Mineração) for donating NbC powders and G. Leal for his technical discussions.

Thanks to Dr. Paola Miselli (Università di Modena e Reggio Emilia) for performing the TG/DTA analyses and to Dr. Miriam Hanusková (Università di Modena e Reggio Emilia) for the particle size distribution analyses.

References

[1] F.H. Stott, High-temperature sliding wear of metals, Tribol. Int. 35 (2002) 489–495, https://doi.org/10.1016/S0301-679X(02)00041-5.

[2] D. Majcherczak, P. Dufrenoy, Y. Berthier, Tribological, thermal and mechanical coupling aspects of the dry sliding contact, Tribol. Int. 40 (2007) 834–843, https://doi.org/10.1016/j.triboint.2006.08.004.

[3] R.J.K. Wood, Tribo-corrosion of coatings: a review, J. Phys. D. Appl. Phys. 40 (2007) 5502–5521, https://doi.org/10.1088/0022-3727/40/18/S10.

[4] K. Holmberg, A. Matthews, H. Ronkainen, Coatings tribology—contact mechanisms and surface design, Tribol. Int. 31 (1998) 107–120, https://doi.org/10.1016/S0301-679X(98)00013-9.

[5] L.-M. Berger, Application of hardmetals as thermal spray coatings, Int. J. Refract. Met. Hard Mater. 49 (2015) 350–364, https://doi.org/10.1016/j.ijrmhm.2014.09.029.

[6] P. Ettmayer, H. Kolaska, H.M. Ortner, History of hardmetals, in: V.K. Sarin, D. Mari, L. Llanes (Eds.), Comprehensive Hard Materials - Volume 1: Hardmetals, Elsevier, Amsterdam, NL, 2014, pp. 3–27, https://doi.org/10.1016/B978-0-08-096527-7.00001-5.

[7] L. Prakash, Fundamentals and general applications of hardmetals, in: V.K. Sarin, D. Mari, L. Llanes (Eds.), Comprehensive Hard Materials - Volume 1: Hardmetals, Elsevier, Amsterdam, NL, 2014, pp. 29–90, https://doi.org/10.1016/B978-0-08-096527-7.00002-7.

[8] Z.Z. Fang, M.C. Koopman, H. Wang, Cemented tungsten carbide hardmetal - an introduction, in: V.K. Sarin, D. Mari, L. Llanes (Eds.), Comprehensive Hard Materials - Volume 1: Hardmetals, Elsevier, Amsterdam, 2014, pp. 123–137, https://doi.org/10.1016/B978-0-08-096527-7.00004-0.

[9] D. Lee, Wear-resistant coatings, in: R.C. Tucker Jr. (Ed.), ASM Handbook - Volume 5A: Thermal Spray Technology, ASM International, Materials Park, OH, USA, OH, USA, 2013, pp. 253–256, https://doi.org/10.31399/asm.hb.v05a.a0005734.

[10] L. Tang, P. Wang, T.E. Graedel, S. Pauliuk, K. Xiang, Y. Ren, W.-Q. Chen, Refining the understanding of China's tungsten dominance with dynamic material cycle analysis, Resour. Conserv. Recycl. 158 (2020), 104829, https://doi.org/10.1016/j.resconrec.2020.104829.

[11] S. van den Brink, R. Kleijn, B. Sprecher, A. Tukker, Identifying supply risks by mapping the cobalt supply chain, Resour. Conserv. Recycl. 156 (2020), 104743, https://doi.org/10.1016/j.resconrec.2020.104743.

[12] C.M. Fernandes, A.M.R. Senos, Cemented carbide phase diagrams: a review, Int. J. Refract. Met. Hard Mater. 29 (2011) 405–418, https://doi.org/10.1016/j.ijrmhm.2011.02.004.

[13] A.F. Guillermet, An assessment of the Fe-Ni-W-C phase diagram, Int. J. Mater. Res. 78 (1987) 165–171, https://doi.org/10.1515/ijmr-1987-780301.

[14] A.S. Kurlov, A.I. Gusev, Phases and Equilibria in the W–C and W–Co–C systems, in: Tungsten Carbides: Structure, Properties and Application in Hardmetals, Springer International Publishing, Cham, Switzerland, 2013, pp. 5–56, https://doi.org/10.1007/978-3-319-00524-9_2.

[15] J. Sun, J. Zhao, F. Gong, X. Ni, Z. Li, Development and application of WC-based alloys bonded with alternative binder phase, Crit. Rev. Solid State Mater. Sci. 44 (2019) 211–238, https://doi.org/10.1080/10408436.2018.1483320.

[16] L.-M. Berger, M. Woydt, S. Saaro, Comparison of self-mated hardmetal coatings under dry sliding conditions up to 600°C, Wear. 266 (2009) 406–416, https://doi.org/10.1016/j.wear.2008.04.013.

[17] Š. Houdková, F. Zahálka, M. Kašparová, L.-M. Berger, Comparative study of thermally sprayed coatings under different types of wear conditions for hard chromium replacement, Tribol. Lett. 43 (2011) 139–154, https://doi.org/10.1007/s11249-011-9791-9.

[18] L.-M. Berger, Hard but slippery - titanium hardmetal coatings have industrial potential, Metal Powder Rep. 60 (2005) 28–31, https://doi.org/10.1016/S0026-0657(05)70410-0.

[19] L.-M. Berger, C.C. Stahr, S. Saaro, S. Thiele, M. Woydt, N. Kelling, Dry sliding up to 7.5m/s and 800°C of thermally sprayed coatings of the TiO2–Cr2O3 system and (Ti,Mo)(C,N)–Ni(Co), Wear 267 (2009) 954–964, https://doi.org/10.1016/j.wear.2008.12.105.

[20] K. Bobzin, M. Öte, M.A. Knoch, X. Liao, J. Sommer, Application of TiC reinforced Fe-based coatings by means of high velocity air fuel spraying, IOP Conf. Ser. Mater. Sci. Eng. 181 (2017), 012014, https://doi.org/10.1088/1757-899X/181/1/012014.

[21] K. Bobzin, T. Schlaefer, K. Richardt, T. Warda, G. Reisel, Investigation of properties and wear behavior of HVOF sprayed TiC-strengthened Fe coatings, J. Therm. Spray Technol. 18 (2009) 672–677, https://doi.org/10.1007/s11666-009-9384-4.

[22] G. Bolelli, A. Colella, L. Lusvarghi, S. Morelli, P. Puddu, E. Righetti, P. Sassatelli, V. Testa, TiC–NiCr thermal spray coatings as an alternative to WC-CoCr and Cr_3C_2–NiCr, Wear. 450–451 (2020), 203273, https://doi.org/10.1016/j.wear.2020.203273.

[23] V. Testa, S. Morelli, G. Bolelli, F. Bosi, P. Puddu, A. Colella, T. Manfredini, L. Lusvarghi, Corrosion and wear performances of alternative TiC-based thermal spray coatings, Surf. Coat. Technol. 438 (2022), 128400, https://doi.org/10.1016/j.surfcoat.2022.128400.

[24] R.M. Genga, P. Rokebrand, L.A. Cornish, N. Nelwalani, G. Brandt, N. Kelling, M. Woydt, A.J. van Vuuren, C. Polese, High-temperature sliding wear, elastic modulus and transverse rupture strength of Ni bonded NbC and WC cermets, Int. J. Refract. Met. Hard Mater. 87 (2020), 105143, https://doi.org/10.1016/j.ijrmhm.2019.105143.

[25] M. Woydt, S. Huang, J. Vleugels, H. Mohrbacher, E. Cannizza, Potentials of niobium carbide (NbC) as cutting tools and for wear protection, Int. J. Refract. Met. Hard Mater. 72 (2018) 380–387, https://doi.org/10.1016/j.ijrmhm.2018.01.009.

[26] E. Uhlmann, D. Hinzmann, K. Kropidlowksi, P. Meier, L. Prasol, M. Woydt, Substitution of commercially coated tungsten carbide tools in dry cylindrical turning process by HiPIMS coated niobium carbide cutting inserts, Surf. Coat. Technol. 354 (2018) 112–118, https://doi.org/10.1016/j.surfcoat.2018.07.105.

[27] G. Bolelli, L.-M. Berger, T. Börner, H. Koivuluoto, L. Lusvarghi, C. Lyphout, N. Markocsan, V. Matikainen, P. Nylén, P. Sassatelli, R. Trache, P. Vuoristo, Tribology of HVOF- and HVAF-sprayed WC–10Co4Cr hardmetal coatings: a comparative assessment, Surf. Coat. Technol. 265 (2015) 125–144, https://doi.org/10.1016/j.surfcoat.2015.01.048.

[28] M. Grohol, C. Veeh, Study on the Critical Raw Materials for the EU 2023 Final Report, Luxembourg, 2023, https://doi.org/10.2873/725585.

[29] C.E.L. Latunussa, K. Georgitzikis, C.T. de Matos, M. Grohol, U. Eynard, D. Wittmer, L. Mancini, M. Unguru, C. Pavel, S. Carrara, F. Mathieux, D. Pennington, G.A. Blengini, Study on the EU's List of Critical Raw Materials (2020), Factsheets on Critical Raw Materials, Luxembourg, 2020. doi:https://doi.org/10.2873/92480.

[30] M. Woydt, H. Mohrbacher, J. Vleugels, S. Huang, Niobium carbide for wear protection – tailoring its properties by processing and stoichiometry, Metal Powder Rep. 71 (2016) 265–272, https://doi.org/10.1016/j.mprp.2015.12.010.

[31] A. Amaya, O. Piamba, J. Olaya, Improvement of corrosion resistance for gray cast iron in palm biodiesel application using thermoreactive diffusion Niobium Carbide (NbC) coating, Coatings. 8 (2018) 216, https://doi.org/10.3390/coatings8060216.

[32] M.O. Rettig, K. Kaesgen, C.M. Verpoort, J. Grochowicz, A. Wank, C. Schmengler, A. Krause, Process for Producing a Protective Coating on a Brake Side of a Brake Disk Main Element And Process for Producing a Brake Disk, US patent 11635117 B2, 2023.

[33] G. Bolelli, A. Colella, L. Lusvarghi, P. Puddu, R. Rigon, P. Sassatelli, V. Testa, Properties of HVOF-sprayed TiC-FeCrAl coatings, Wear. 418–419 (2019) 36–51, https://doi.org/10.1016/j.wear.2018.11.002.

[34] V. Testa, S. Morelli, G. Bolelli, B. Benedetti, P. Puddu, P. Sassatelli, L. Lusvarghi, Alternative metallic matrices for WC-based HVOF coatings, Surf. Coat. Technol. 402 (2020), 126308, https://doi.org/10.1016/j.surfcoat.2020.126308.

[35] ISO 14577-1:2002, Metallic materials — Instrumented indentation test for hardness and materials parameters — part 1: test method, in: International Organization for Standardization (ISO), Geneva, Switzerland, 2002.

[36] T. Teppernegg, T. Klünsner, C. Kremsner, C. Tritremmel, C. Czettl, S. Puchegger, S. Marsoner, R. Pippan, R. Ebner, High temperature mechanical properties of WC–Co hard metals, Int. J. Refract. Met. Hard Mater. 56 (2016) 139–144, https://doi.org/10.1016/j.ijrmhm.2016.01.002.

[37] J.B. Wachtman, D.G. Lam, Young's Modulus of various refractory materials as a function of temperature, J. Am. Ceram. Soc. 42 (1959) 254–260, https://doi.org/10.1111/j.1151-2916.1959.tb15462.x.

[38] S. Mahade, A. Mulone, S. Björklund, U. Klement, S. Joshi, Investigating load-dependent wear behavior and degradation mechanisms in Cr_3C_2–NiCr coatings deposited by HVAF and HVOF, J. Mater. Res. Technol. 15 (2021) 4595–4609, https://doi.org/10.1016/j.jmrt.2021.10.088.

[39] Z. Russell, W.A. Sparling, T.L. Stewart, P. Gray, M. Gaier, M.J. Froning, G. Mazzanti, K.P. Plucknett, Gelation-based feed-stock technologies for HVOF thermal spray development: Micro-composite powder preparation and HVOF coating microstructure, Surf. Coat. Technol. 452 (2023), 129089, https://doi.org/10.1016/j.surfcoat.2022.129089.

[40] M.S. El-Eskandarany, Utilization of ball-milled powders for surface protective coating, in: Mechanical Alloying, Elsevier, 2020, pp. 309–334, https://doi.org/10.1016/B978-0-12-818180-5.00012-1.

[41] S. Sauceda, S. Lascano, J. Núñez, C. Parra, C. Arévalo, L. Béjar, Effect of HVOF processing parameters on Cr_3C_2-NiCr hard coatings deposited on AISI 4140 steel, Eng. Sci. Technol. 39 (2023), 101342, https://doi.org/10.1016/j.jestch.2023.101342.

[42] H. Chen, M. Fan, L. Li, W. Zhu, H.N. Li, J. Li, Y. Yin, Effects of internal oxide contents on the oxidation and β-phase depletion behaviour in HOVF CoNiCrAlY coatings, Surf. Coat. Technol. 424 (2021), 127666, https://doi.org/10.1016/j.surfcoat.2021.127666.

[43] S. Deshpande, S. Sampath, H. Zhang, Mechanisms of oxidation and its role in microstructural evolution of metallic thermal spray coatings - case study for Ni-Al, Surf. Coat. Technol. 200 (2006) 5395–5406, https://doi.org/10.1016/j.surfcoat.2005.07.072.

[44] C.J. Li, G.C. Ji, Y.Y. Wang, K. Sonoya, Dominant effect of carbide rebounding on the carbon loss during high velocity oxy-fuel spraying of Cr_3C_2-NiCr, Thin Solid Films 419 (2002) 137–143, https://doi.org/10.1016/S0040-6090(02)00708-3.

[45] J.A. Picas, M. Punset, S. Menargues, M. Campillo, M. Teresa Baile, A. Forn, The influence of heat treatment on tribological and mechanical properties of HVOF sprayed CrC–NiCr coatings, Int. J. Mater. Form. 2 (2009) 225–228, https://doi.org/10.1007/s12289-009-0466-0.

[46] K. Palanisamy, S. Gangolu, J. Mangalam Antony, Effects of HVOF spray parameters on porosity and hardness of 316L SS coated Mg AZ80 alloy, Surf. Coat. Technol. 448 (2022), 128898, https://doi.org/10.1016/j.surfcoat.2022.128898.

[47] I. Baumann, L. Hagen, W. Tillmann, P. Hollingsworth, D. Stangier, G. Schmidtmann, M. Tolan, M. Paulus, C. Sternemann, Process characteristics, particle behavior and coating properties during HVOF spraying of conventional, fine and nanostructured WC-12Co powders, Surf. Coat. Technol. 405 (2021), 126716, https://doi.org/10.1016/j.surfcoat.2020.126716.

[48] E. Rabinowicz, The Wear coefficient—magnitude, scatter, uses, J. Lubr. Technol. 103 (1981) 188–193, https://doi.org/10.1115/1.3251624.

[49] G. Straffelini, Friction, in: Friction and Wear - Methodologies for Design and Control, Springer International Publishing, Cham, Switzerland, 2015, pp. 21–60, https://doi.org/10.1007/978-3-319-05894-8_2.

[50] J.P. Peña, P. Bouvier, O. Isnard, Structural properties and Raman spectra of columbite-type $NiNb_{2-x}V_xO_6$ synthesized under high pressure, J. Solid State Chem. 291 (2020), 121607, https://doi.org/10.1016/j.jssc.2020.121607.
[51] D. Manzani, T. Gualberto, J.M.P. Almeida, M. Montesso, C.R. Mendonça, V.A. G. Rivera, L. De Boni, M. Nalin, S.J.L. Ribeiro, Highly nonlinear $Pb_2P_2O_7$-Nb_2O_5 glasses for optical fiber production, J. Non-Cryst. Solids 443 (2016) 82–90, https://doi.org/10.1016/j.jnoncrysol.2016.04.019.
[52] M.F. Daniel, B. Desbat, J.C. Lassegues, B. Gerand, M. Figlarz, Infrared and Raman study of WO_3 tungsten trioxides and $WO_3{\cdot}xH_2O$ tungsten trioxide tydrates, J. Solid State Chem. 67 (1987) 235–247, https://doi.org/10.1016/0022-4596(87)90359-8.
[53] S.G. Huang, J. Vleugels, H. Mohrbacher, M. Woydt, Densification and tribological profile of niobium oxide, Wear. 352–353 (2016) 65–71, https://doi.org/10.1016/j.wear.2016.02.003.
[54] M. Woydt, H. Mohrbacher, Friction and wear of binder-less niobium carbide, Wear. 306 (2013) 126–130, https://doi.org/10.1016/j.wear.2013.07.013.
[55] M. da Cunha Belo, M. Walls, N.E.E. Hakiki, J. Corset, E. Picquenard, G. Sagon, D. Noël, Composition, structure and properties of the oxide films formed on the stainless steel 316L in a primary type PWR environment, Corros. Sci. 40 (1998) 447–463, https://doi.org/10.1016/S0010-938X(97)00158-3.
[56] M. Woydt, H. Mohrbacher, The use of niobium carbide (NbC) as cutting tools and for wear resistant tribosystems, Int. J. Refract. Met. Hard Mater. 49 (2015) 212–218, https://doi.org/10.1016/j.ijrmhm.2014.07.002.
[57] M. Woydt, H. Mohrbacher, The tribological and mechanical properties of niobium carbides (NbC) bonded with cobalt or Fe_3Al, Wear. 321 (2014) 1–7, https://doi.org/10.1016/j.wear.2014.09.007.
[58] G. Bolelli, L.-M. Berger, T. Börner, H. Koivuluoto, V. Matikainen, L. Lusvarghi, C. Lyphout, N. Markocsan, P. Nylén, P. Sassatelli, R. Trache, P. Vuoristo, Sliding and abrasive wear behaviour of HVOF- and HVAF-sprayed Cr_3C_2–NiCr hardmetal coatings, Wear. 358–359 (2016) 32–50, https://doi.org/10.1016/j.wear.2016.03.034.
[59] J.K.N. Murthy, B. Venkataraman, Abrasive wear behaviour of WC-CoCr and Cr_3C_2-20(NiCr) deposited by HVOF and detonation spray processes, Surf. Coat. Technol. 200 (2006) 2642–2652, https://doi.org/10.1016/j.surfcoat.2004.10.136.
[60] L.A. Luiz, J. de Andrade, C.M. Pesqueira, I.B. de A.F. Siqueira, G.B. Sucharski, M. J. de Sousa, Corrosion behavior and galvanic corrosion resistance of WC and Cr_3C_2 cermet coatings in Madeira River Water, J. Therm. Spray Technol. 30 (2021) 205–221, https://doi.org/10.1007/s11666-021-01152-8.
[61] P. Suresh Babu, Y. Madhavi, L. Rama Krishna, D. Srinivasa Rao, G. Padmanabham, Thermally-sprayed WC-based cermet coatings for corrosion resistance applications, JOM. 70 (2018) 2636–2649, https://doi.org/10.1007/s11837-018-3131-6.
[62] S. Sutthiruangwong, G. Mori, Corrosion properties of co-based cemented carbides in acidic solutions, Int. J. Refract. Met. Hard Mater. 21 (2003) 135–145, https://doi.org/10.1016/S0263-4368(03)00027-1.
[63] S.G. Huang, K. Vanmeensel, H. Mohrbacher, M. Woydt, J. Vleugels, Microstructure and mechanical properties of NbC-matrix hardmetals with secondary carbide addition and different metal binders, Int. J. Refract. Met. Hard Mater. 48 (2015) 418–426, https://doi.org/10.1016/j.ijrmhm.2014.10.014.
[64] S.G. Huang, J. Vleugels, H. Mohrbacher, M. Woydt, Microstructure and mechanical properties of NbC matrix cermets using Ni containing metal binder, Metal Powder Rep. 71 (2016) 349–355, https://doi.org/10.1016/j.mprp.2016.05.009.
[65] S. Huang, P. Baets, J. Sukumaran, H. Mohrbacher, M. Woydt, J. Vleugels, Effect of carbon content on the microstructure and mechanical properties of NbC-Ni based cermets, Metals. 8 (2018) 178, https://doi.org/10.3390/met8030178.